Check for updates

ADVANCED ENERGY MATERIALS
www.advenergymat.de

Closed-Loop Iodine-Oxygen Electrochemistry for High-Reversibility Neutral Zinc–Air Hybrid Batteries

Jie Chen, Wanfang Li, Ruoxuan Sun, Lei Yan, Shikun Li,* Zhuying Xu,* Xuezhi Zeng, and Yong Hu**

Neutral Zn–air batteries offer advantages in dendrite suppression and carbonation resistance, however, their performance is limited by high overpotentials resulting from insulating discharge products and sluggish oxygen kinetics. Herein, a closed-loop iodide-oxygen cycle mechanism for a neutral aqueous Zn–air/iodide hybrid battery (ZAIB), integrating oxygen and iodide redox chemistry, is proposed. A multifunctional electrocatalyst, featuring FeN nanoparticles anchored on a hierarchically porous carbon matrix, is designed to drives oxygen reduction reactions (ORR) and iodide oxidation/reduction reactions (IOR/IRR). This catalyst spatially confines zinc hydroxyacetate dihydrate (ZHA) precipitates within its honeycomb meso-macroporous framework, thereby preserving triple-phase boundaries. During discharge, I^- generated from I_3^- reduction enhances the kinetics, thereby increasing discharge voltage. Concurrently, OH^- formed during ORR reacts with the electrolyte to produce ZHA. Upon charging, thermodynamically favored low-potential IOR dominates, regenerating I_3^- from I^- and decomposing ZHA to release OH^-. The released OH^- then spontaneously reacts with I_3^- to regenerate I^- and evolve O_2, resulting in a reduced charge voltage. Consequently, the neutral ZAIB achieves a low charge/discharge voltage gap (640.1 mV), high energy efficiency (54.0%), and exceptional stability (>1800 h at 2 mA cm^{-2}). This synergistic mediator-catalyst codesign strategy offers a viable pathway to high-performance neutral metal–air systems.

1. Introduction

Zinc–air batteries (ZABs) are emerging as one of the most promising next-generation energy storage systems due to their high theoretical energy density, safety, environmental benefits, and economic viability.[1] Despite significant advancements in developing zinc anodes and electrocatalyst cathodes, the usage of strong bases as the electrolytes leads to chemical instability and poor electrochemical reversibility of traditional ZABs.[2] Additionally, the slow kinetics of oxygen electrocatalysis, particularly the oxygen evolution reaction (OER) at the cathode, results in a significant charge–discharge voltage gap, with charge voltage above 2.0 V and low energy efficiency (typically below 50%) (**Scheme 1**).[3] Elevated charge voltages also can accelerate cathode oxidation and degradation, leading to battery failure.

To address these limitations, significant efforts have been dedicated to incorporating easily oxidizable substances (such as ethanol, urea, glucose, etc.) with more favorable thermodynamics into the

J. Chen, W. Li, R. Sun, Z. Xu
Key Laboratory of the Ministry of Education for Advanced Catalysis Materials
Department of Chemistry
Zhejiang Normal University
Jinhua 321004, China
E-mail: zhuyingxu@zjnu.edu.cn

L. Yan, Y. Hu
Institute of Nanocatalysis and Energy Conversion
College of Chemistry and Materials Engineering
Zhejiang A&F University
Hangzhou 311300, China
E-mail: leiyan@zafu.edu.cn; yonghu@zafu.edu.cn, yonghu@zjnu.edu.cn

S. Li
Xinjiang Key Laboratory of Coal Clean Conversion & Chemical Engineering Process
School of Chemical Engineering and Technology
Xinjiang University
Urumqi 830046, China
E-mail: shikunli@xju.edu.cn

X. Zeng
School of Chemical Engineering and Light Industry
Guangdong University of Technology
GuangZhou 510006, China

The ORCID identification number(s) for the author(s) of this article can be found under https://doi.org/10.1002/aenm.202503298

DOI: 10.1002/aenm.202503298

 © 2025 Wiley-VCH GmbH

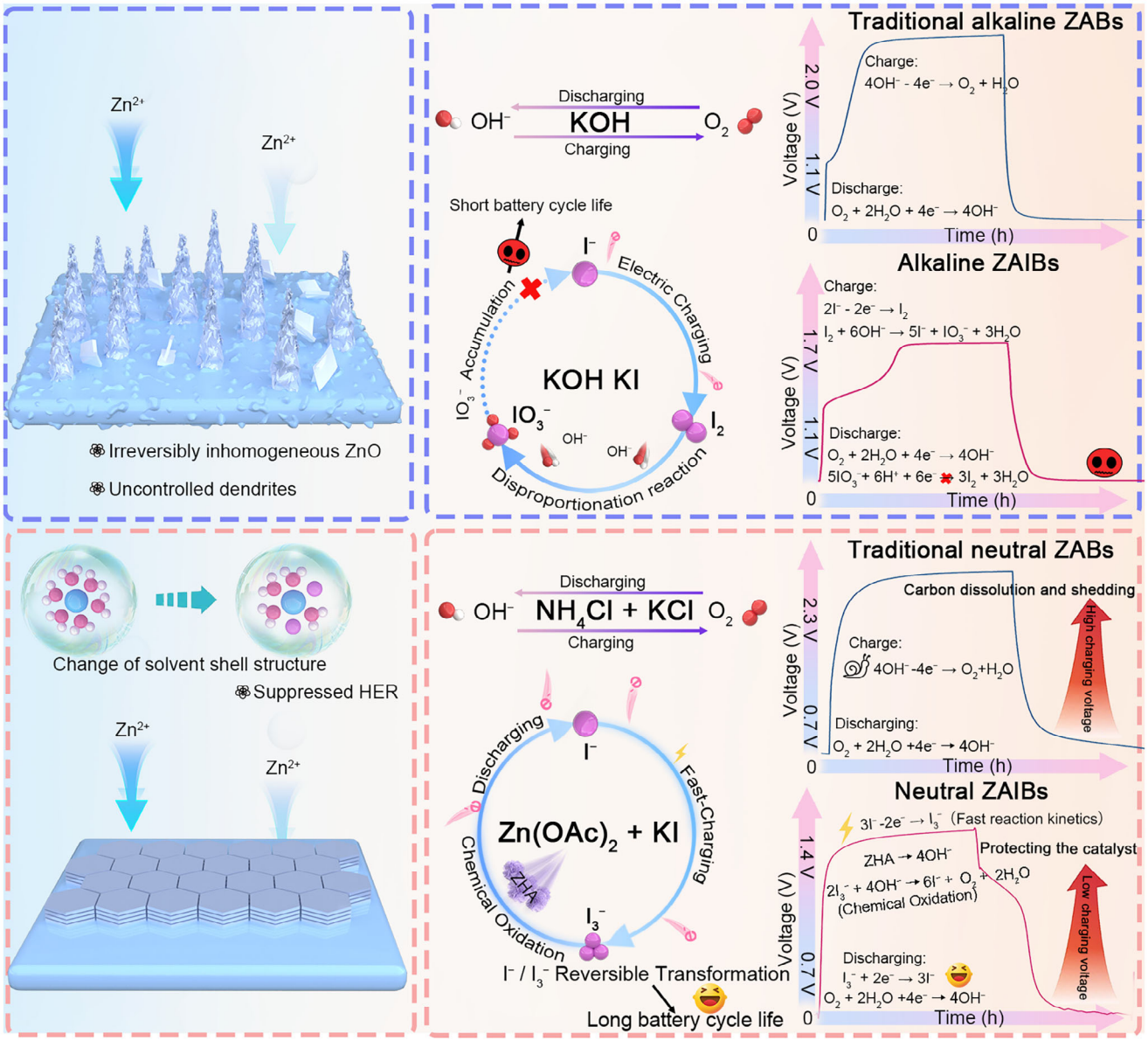

Scheme 1. Schematic diagram of the difference between the conventional batteries and the proposed neutral ZAIBs. Overview of alkaline ZABs with KOH electrolyte, alkaline ZAIBs with KOH/KI electrolyte, neutral ZABs with NH_4Cl/KCl electrolyte, and neutral ZAIBs with $Zn(OAc)_2$/KI electrolyte. ZHA refers to zinc hydroxyacetate dihydrate ($Zn_5(OH)_8(CH_3CO_2)_2{\cdot}2H_2O$).

electrolyte as reaction modifiers, forming zinc–air hybrid batteries.[4] Notably, potassium iodide (KI) is used to construct zinc–air/iodide hybrid batteries (ZAIBs), which improve energy efficiency and cycle stability by employing alternative iodide oxidation reaction (IOR) with accelerated kinetics and reduced oxidation potential to replace the sluggish OER pathway.[5] Due to the lower charge voltages, these ZAIBs hold the potential for fast charging and are suitable for applications in the electric vehicle industry.[6] However, most reported ZAIBs operate in alkaline conditions, where intermediate I_2 produced during charging undergoes disproportionation, forming I^- and stable IO_3^-.[7] The reduction of IO_3^- to I^- follows a complex 6-electron pathway, which increases the difficulty of sustaining iodine species cycle.[8] Some attempts have been made to improve the reversible cycling of iodine species. For instance, Sun et al. developed a Fe-Co diatomic site catalyst for I^-/IO_3^- redox, achieving high energy efficiency of alkaline ZAIBs.[9] Still, the cycle life of battery remains short (less than 500 h), significantly limiting its practical application. Besides, Huang et al. demonstrated organic ZAIBs using ethylene glycol electrolyte with accelerated kinetics via reversible I_3^-/I^- redox, achieving improved cycling efficiency (56.03% at 0.4 mA cm^{-2}) and extended cycle life (1300 h).[10] However, organic electrolytes are unfavorable to oxygen electrocatalysis due to poor ion transport and reaction kinetics, which diminishes capacity and output power of battery, particularly at high current densities.[11] Thus, reversible iodine conversion electrochemistry

© 2025 Wiley-VCH GmbH

under simple and feasible conditions, while retaining the advantages of aqueous ZABs, is crucial for realizing ZAIBs with high energy efficiency and long lifespan.

Previous studies have reported that the corrosion of zinc plates and carbon is significantly reduced in a neutral aqueous electrolyte, and the solution does not absorb carbon dioxide from the air to form carbonates. The absence of OH^- can drastically lower the concentration of $Zn(OH)_4^{2-}$, which facilitates uniform Zn^{2+} deposition and suppresses zinc dendrite formation, ultimately improving the stability of neutral ZABs.[12] However, a core challenge under neutral conditions is the sluggish kinetics of oxygen reactions coupled with the irreversible accumulation of low-conductivity discharge byproducts, which both impair catalytic performance and reduce battery output. For instance, Wang's work demonstrated that OH^- generated from the ORR reacts with zinc sulfate ($ZnSO_4$) to form $Zn_4(OH)_6SO_4{\cdot}0.5H_2O$ (ZHS), and this process is limited by the availability of $ZnSO_4$ or H_2O in the electrolyte. And after charging, it can continuously consume $ZnSO_4$ and degrade cycling performance owing to the presence of the residual insulating ZHS flakes.[13] Similarly, Sun et al. reported that the use of zinc acetate ($Zn(OAc)_2$) electrolyte for ZABs would produce zinc hydroxyacetate dihydrate ($Zn_5(OH)_8(CH_3CO_2)_2{\cdot}2H_2O$, ZHA) during discharge.[14] These poorly reversible solid discharge byproducts will continue to accumulate at the interface, hindering mass transport and covering active cathode sites, resulting in high overpotentials during both charge and discharge.

Inspired by the rapid redox reaction and high output voltage (1.29 V vs Zn/Zn^{2+}) in zinc–iodine (Zn–I_2) batteries,[15] we propose the novel concept of neutral aqueous ZAIBs that incorporate the I_3^-/I^- redox reaction into neutral electrolytes, facilitating fast charging and discharging as well as extending cycle time. The high theoretical specific capacity of iodine coupled with the zinc–air system, significantly improves active material utilization and enhances the energy density of the assembled cell. During discharge, both oxygen and iodine can simultaneously participate in redox reactions, enabling multielectron transfer processes that overcome the capacity limitations of Zn-I_2 batteries.[3,16] Meanwhile, we expect to utilize the chemical oxidation of I_3^- with OH^- to accelerate the decomposition of discharging byproducts. To make neutral aqueous ZAIBs competitive, three key developments are needed: i) electrocatalysts capable of effective oxygen evolution/reduction and I^-/I_3^- redox under neutral conditions while featuring optimized structures to mitigate the impact of discharge solid products; ii) the electrolytes with high ionic conductivity that enhance reversibility of the zinc anode and catalytic kinetics of cathode; and iii) deep insights into the theoretical mechanisms for reversible ZAIB reactions. Nevertheless, the design of highly efficient multifunctional catalysts under neutral conditions remains rare, and the systematic development of neutral aqueous ZAIBs has been hindered by a limited understanding of the relationship between iodine transformation and oxygen reduction/oxidation mechanisms.

In this work, a highly reversible neutral aqueous ZAIB is designed and realized through iodide-oxygen coupling redox chemistry for the first time. FeN nanoparticles anchored on the honeycomb-like porous carbon (FeN-HNPC) are fabricated as a multifunctional electrocatalyst, demonstrating superior catalytic activity toward oxygen reduction reaction (ORR), IOR and iodine reduction reaction (IRR) across neutral and alkaline media, while the spatial confinement of insulating ZHA precipitate within this architecture stabilizes the triple-phase interface and mitigates detrimental effects on charge transfer kinetics and stability. Furthermore, high ionic conductivity and suppression of zinc dendrite growth can be achieved via the usage of neutral $Zn(OAc)_2$ electrolyte containing KI. In situ Raman spectroscopy, ultraviolet (UV) spectrophotometry, and density functional theory (DFT) calculations confirm the high reversibility of the iodide-oxygen coupling mechanism during the charge–discharge process in neutral electrolyte. During discharging, I^- is produced via the reduction of I_3^-, which promotes the ORR kinetics and increases the discharge voltage. The OH^- ion formed during ORR further reacts with the electrolyte to form zinc hydroxyacetate dihydrate ($Zn_5(OH)_8(CH_3CO_2)_2{\cdot}2H_2O$, ZHA) at the catalyst surface. During charging, I^- is preferentially oxidized to I_3^-, while ZHA partially decomposes to release OH^-. The liberated OH^- then spontaneously reacts with I_3^- to regenerate I^- and evolve O_2. The closed-loop iodide-oxygen cycle and reversible ZHA conversion mechanism allow the neutral ZAIBs to operate at a low charge voltage of 1.38 V, a voltage gap of only 640.1 mV, a high energy efficiency of 54.0% and an extended cycle life of over 1800 h at 2 mA cm^{-2}. These findings provide valuable insights into the development of high-performance neutral metal–air systems.

2. Results and Discussion

2.1. Design of Multifunctional Electrocatalyst

Fe-N-C-based materials have demonstrated great potential in oxygen and iodide electrocatalysis.[4b] However, the strong binding to oxygen intermediates and weak binding to iodine intermediates at active Fe centers limit the multifunctional catalytic performance of Fe-N-C materials. Introducing FeN nanoparticles as charge regulators is expected to modify the electronic structure of the active sites, potentially adjusting the adsorption capacity of Fe sites. To understand the electrochemical performance potential, models of FeNC coupled with FeN nanoparticles (FeN@FeNC) and pure FeNC were constructed, as shown in Figure S1 (Supporting Information).[17] Since *OH, I^- and I_3^- are key intermediates in oxygen redox and iodine redox processes, the charge density difference and Bader charge transfer analyses were calculated to gain insights into electron redistribution (**Figure 1a–c**). Optimized charge density difference patterns of FeN@FeNC and FeNC are presented as colored isosurfaces. FeN@FeNC exhibits lower electron transfer to *OH (1.03 e^-) than FeNC (1.05 e^-). In FeNC, this charge transfer is primarily localized at the interface, enhancing OH binding strength. It indicates that the introduction of FeN nanoparticles weakens the adsorption of OH^- on the site, which is favorable for oxygen catalytic activity.[15b] On the other hand, FeN@FeNC transfers 0.43 e^- and 0.69 e^- to I^- and I_3^-, respectively, which is much higher than the electron transfer by pure FeNC (0.38 e^- for I^-, 0.58 e^- for I_3^-), indicating stronger adsorption of iodide intermediates on FeN@FeNC.[18] The selective optimization of intermediates adsorption significantly lowers the reaction barriers during oxygen and iodine catalysis, enhancing multifunctional catalytic activity for FeN@FeNC.[19]

The calculated Gibbs free energy diagrams for ORR and OER were investigated based on the constructed FeN@FeNC and

© 2025 Wiley-VCH GmbH

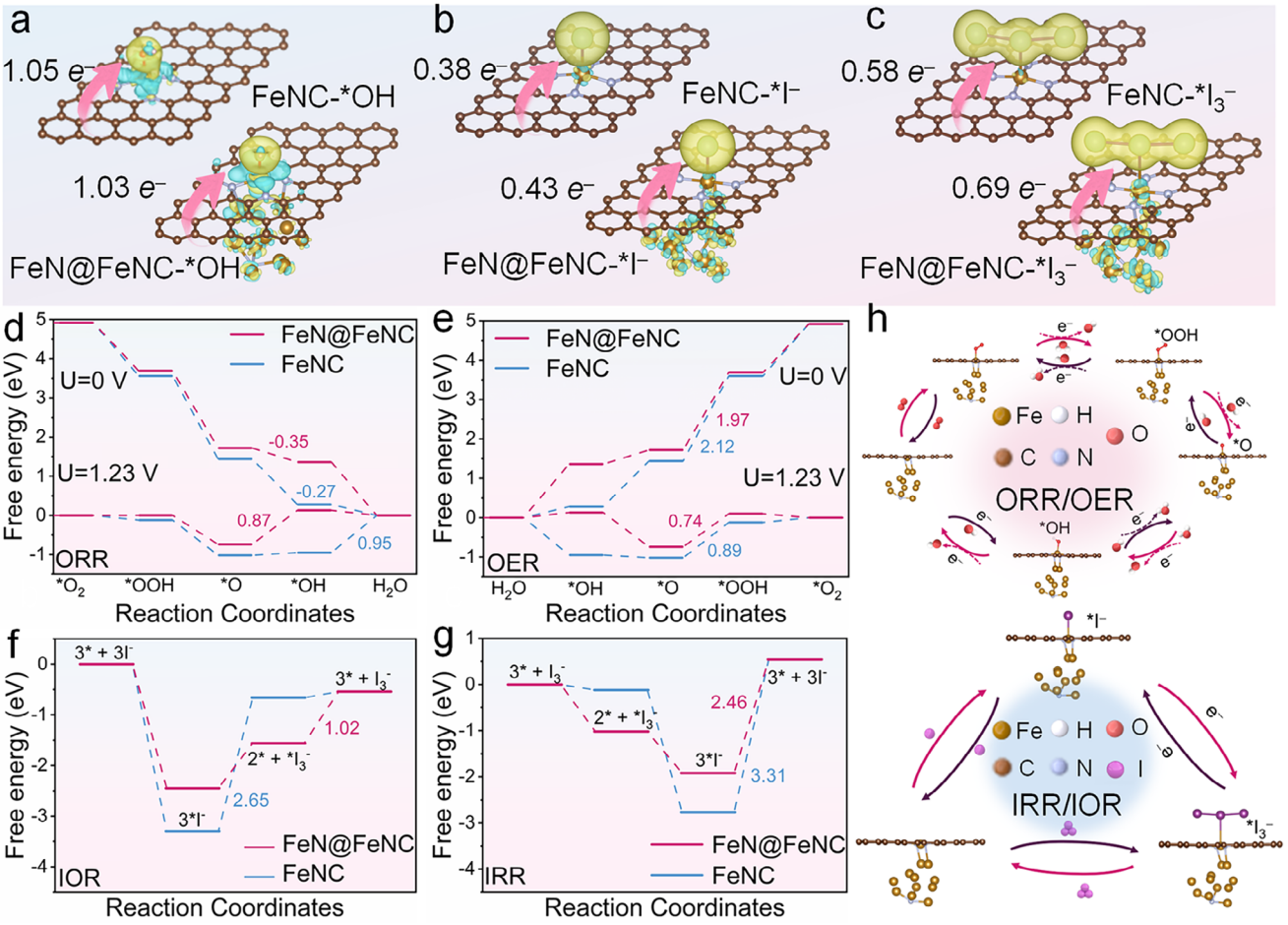

Figure 1. Prediction of the multifunctional electrocatalytic behaviors. Charge density difference patterns of a) *OH, b) I^-, and c) I_3^- on FeN@FeNC and FeNC (yellow color denotes electron accumulation, and cyan color represents electron depletion). d) ORR and e) OER free energy diagrams of FeN@FeNC and FeNC at $U = 0$ V and $U = 1.23$ V. f) IOR and g) IRR free energy diagrams of FeN@FeNC and FeNC. h) The optimized adsorption configurations of oxygen intermediates ($*O_2$, *OH, *O, and *OOH) and iodine intermediates ($*I^-$ and $*I_3^-$) on the interface.

FeNC models according to Equations (S1–S8) (Figure S2, Supporting Information). For ORR (Figure 1d), all reaction steps are exothermic with downhill energetics for FeN@FeNC and FeNC at the zero electrode potential ($U = 0$ V vs RHE), verifying these catalysts are favorable for ORR. At equilibrium potential ($U = 1.23$ V), FeNC shows the highest free energy change ($\Delta G = 0.95$ eV) in the final elementary step (protonation of *OH to H_2O), while FeN@FeNC exhibits a lower rate-determining step (RDS) in the third elementary step (protonation of *O to *OH) of 0.87 eV, highlighting the facilitative role of FeN@FeNC in ORR. In OER, the ΔG for *O → *OOH on FeN@FeNC is 1.97 eV at $U =$ 0 V (Figure 1e), which is lower than that of FeNC (2.12 eV). At U = 1.23 V, the RDS exhibits reaction free-energy barrier of 0.74 and 0.89 eV for FeN@FeNC and FeNC, respectively, demonstrating that FeN nanoparticles effectively decrease the OER energy barrier. In addition, the Gibbs free energies were calculated for I^- oxidation and I_3^- reduction pathways of FeN@FeNC and FeNC (Figure S3, Supporting Information). In the electrocatalytic IOR and IRR (Figure 1f,g), the initial step involves the adsorption of free iodine species onto the catalysts, with negative adsorption energies suggesting thermodynamically favorable processes for I^- and I_3^- adsorption. In the subsequent IOR process (Figure 1f), FeN@FeNC exhibits an RDS step of $*I_3^-$ desorption with energy barriers of 1.02 eV, which is much lower than the limiting barrier of FeNC (RDS is $*I^- \rightarrow *I_3^-$ for 2.65 eV), indicating enhanced catalytic efficiency with the introduction of FeN. The RDS of IRR on FeN@FeNC related to the desorption process of $*I^-$ (2.46 eV) is lower than that of FeNC (3.31 eV), suggesting FeN@FeNC exhibits superior electrocatalytic activity for the IRR (Figure 1g). These conclusions confirm that coupling between FeN nanoparticles and FeNC can effectively optimize the electronic structures of Fe centers, therefore enhancement of ORR, OER, IOR, and IRR activities (Figure 1h), which provide a solid basis for the design of multifunctional catalysts for ZAIBs.

2.2. Synthesis and Characterization of the FeN-HNPC Electrocatalyst

The multifunctional FeN-HNPC electrocatalyst was synthesized using a prefabricated Fe-N coordination strategy, as illustrated in **Figure** 2a (details see the Experimental Section). The synthetic

© 2025 Wiley-VCH GmbH

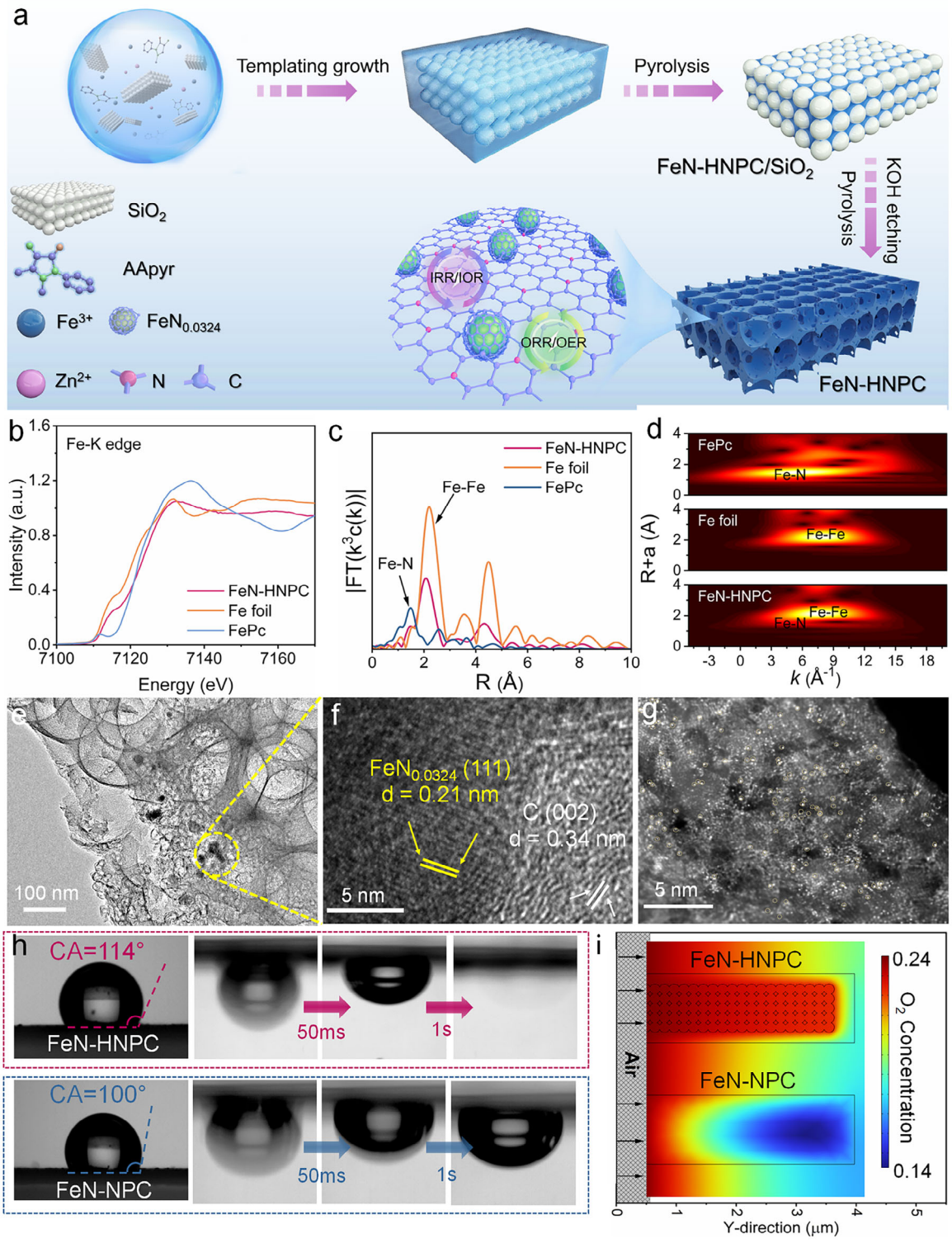

Figure 2. Structural characterizations of the FeN-HNPC electrocatalyst. a) Synthetic procedure of the FeN-HNPC. b) Normalized Fe K-edge XANES spectra. c) FT-EXAFS spectra in *R*-space for FeN-HNPC with the Fe foil and FePc reference samples. d) WT-EXAFS plots of FeN-HNPC with the Fe foil and FePc reference samples. e) TEM image, f) HRTEM image, g) AC-HAADF-STEM image of the FeN-HNPC. h) The measured surface contact angles and O_2 bubbles adhesion behavior evolution on the surfaces at the FeN-HNPC and FeN-NPC electrodes. i) COMSOL Multiphysics Modeling of O_2 diffusion into the FeN-HNPC and FeN-NPC air electrode.

© 2025 Wiley-VCH GmbH

process involves the pyrolysis of aminoantipyrine (AAPyr) and Fe/Zn salts, followed by the etching treatment to remove silica (Figure S4, Supporting Information).[20] The X-ray diffraction (XRD) pattern of the FeN-HNPC (Figure S5, Supporting Information) shows three diffraction peaks at 43°, 50°, and 74°, corresponding to the (111), (200), and (220) planes of cubic iron nitride ($FeN_{0.0324}$, JCPDS No.75-2127), demonstrating the successful construction of FeN nanoparticles. The formation of iron nitride may be attributed to the nitrogen-rich environment provided by the pyrolysis of AAPyr ligand, coupled with the spatial confinement effect of the SiO_2 matrix, which synergistically promotes the nitridation of Fe species.[21] X-ray photoelectron spectroscopy (XPS) further confirms the chemical states of Fe and N elements in the FeN-HNPC (Figure S6, Supporting Information). The Fe content in the FeN-HNPC is 0.89 at%, which is close to that of FeN-NPC (0.84 at%) (Table S1, Supporting Information). The Fe 2p spectra of FeN-HNPC and FeN-NPC (Figure S7, Supporting Information) reveal the peaks at 707.1 and 720.2 eV corresponding to Fe nitrides. The Fe (II) and Fe (III) of FeN_x configurations can also be observed, with the peaks occurring at nearly Fe $2p_{3/2}$ (710.4 and 715.0 eV) and Fe $2p_{1/2}$ (723.5 and 728.1 eV).[22] Additionally, the N 1s high-resolution spectra of the FeN-HNPC and FeN-NPC (Figure S8, Supporting Information) display four distinct peaks at 398.3, 399.6, 400.5, and 402.5 eV, corresponding to pyridinic-N, metal (Fe)-N, pyrrolic-N, and graphitic-N, respectively, indicating the presence of Fe—N bonds in both catalysts.[23] To further identify the local electronic and geometric structures of the Fe species, X-ray absorption fine structure (XAFS) measurements were also performed. The X-ray absorption near-edge structure (XANES) spectra (Figure 2b) of FeN-HNPC exhibit features compared to Fe foil and FePc, reflecting differences in atomic structures. The near-edge absorption energy of Fe is positioned between those of Fe foil and FePc, suggesting the iron valence state lies between 0 and +2. The *R*-space data of k^3 weighted Fe K-edge Fourier-transformed extended X-ray absorption fine structure (FT-EXAFS) spectra reveal two distinct peaks at about 1.5 and 2.1 Å (Figure 2c), corresponding to the Fe-N and Fe-Fe scattering paths, respectively.[24] The wavelet transform (WT)-EXAFS contour plots (Figure 2d) further show maximum intensity at ≈5 $Å^{-1}$ for Fe-N coordination and ≈8 $Å^{-1}$ for Fe-Fe coordination.[25] Additionally, quantitative FT-EXAFS fitting results are provided in Table S2 (Supporting Information).

Scanning electron microscopy (SEM, Figure S9a, Supporting Information) image reveals that the morphology of the FeN-HNPC catalyst has a semiopen honeycomb-like configuration with an average pore size of ≈200 nm. The HNPC sample also exhibits a similar honeycomb structure, whereas the FeN-NPC presents a smoother surface (Figure S9b,c, Supporting Information). Transmission electron microscopy (TEM) image of the FeN-HNPC (Figure 2e) further reveals that nanoparticles are embedded in interconnected porous carbon structures. High-resolution TEM (HRTEM) image (Figure 2f) shows lattice fringes with spacings of 0.21 and 0.34 nm, corresponding to the (111) crystallographic facets of $FeN_{0.0324}$ and the (002) plane of graphitic carbon, respectively. Moreover, aberration-corrected high-angle annular dark-field scanning TEM (AC-HAADF-STEM) confirms the presence of atomically dispersed Fe sites (Figure 2g), observed as bright, isolated dots (highlighted in yellow) with sub-angstrom resolution. These results demonstrate the coexistence of $FeN_{0.0324}$ nanoparticles and single-atom Fe-N_x sites in the FeN-HNPC catalyst. The selected area electron diffraction (SAED) pattern comprises four concentric rings, which can be attributed to the graphitic carbon and $FeN_{0.0324}$, respectively (Figure S10, Supporting Information). Elemental mapping demonstrates the uniform distribution of Fe, N, and C across the FeN-HNPC catalyst (Figure S11, Supporting Information). In addition, the graphitization degree of the as-prepared samples was further investigated by Raman spectroscopy. The relative peak intensity ratio of D and G bands (I_D/I_G) for the FeN-HNPC catalyst is calculated to be 1.01 (Figure S12, Supporting Information), higher than that of the FeN-NPC (0.96) and HNPC (0.98), indicating more carbon defects are generated in the FeN-HNPC sample.[26]

The porous characteristics of the FeN-HNPC were further identified by the·N_2 adsorption/desorption isotherms. The Brunauer–Emmett–Teller specific surface area of the FeN-HNPC catalyst is found to be 522.6 $m^2\ g^{-1}$ (Table S3, Supporting Information), which is significantly higher than those of the FeN-NPC (464.2 $m^2\ g^{-1}$) and HNPC (60.6 $m^2\ g^{-1}$) samples (Figure S13, Supporting Information). Additionally, the pore size distribution of the FeN-HNPC exhibits a greater volume of mesopores, ranging from 3 to 8 nm, in comparison to the FeN-NPC and HNPC samples, which may be contributed by the combined effects of Zn evaporation and SiO_2 etching.[27] The large specific surface area and hierarchical pores provide abundant active sites and facilitate mass transfer at the interface.[28] To further investigate these features, the wettability and oxygen diffusion capabilities of the as-prepared catalysts were examined. As shown in Figure 2h, both the FeN-HNPC and FeN-NPC exhibit hydrophobicity, with contact angles of 114° and 100°, respectively. However, captive bubble measurements show that oxygen diffusion at the honeycomb-shaped FeN-HNPC is faster than that of the bulk FeN-NPC, indicating the contribution of the honeycomb structure to oxygen diffusion.[29] Specifically, oxygen bubbles released into the electrolyte diffuse immediately after 1 s in the FeN-HNPC electrode, while they remain attached to the FeN-NPC surface during the same period. The effective diffusion coefficient of oxygen within the FeN-HNPC catalyst layer is calculated to be $3.3 \times 10^{-8}\ m^{-2}\ s^{-1}$ according to Equations (S9–S12), Supporting Information considerably higher than that of the FeN-NPC sample ($2.3 \times 10^{-8}\ m^{-2}\ s^{-1}$) (Figure S14, Supporting Information).[30] The COMSOL Multiphysics finite element method (FEM) solver was conducted to simulate the effect of the morphological structure on air (oxygen) diffusion. The resulting gaseous oxygen concentration contour plot (Figure 2i) depicts that the electrode geometries resembling the FeN-HNPC can reduce gaseous oxygen transfer resistance, leading to higher oxygen concentration within the honeycomb pores. Conversely, the bulk FeN-NPC obstructs oxygen diffusion into the interior of the catalyst. Therefore, the semiopen honeycomb structure of the FeN-HNPC, combined with a large specific surface area, creates an optimal interface environment for electrochemical reactions.

2.3. Electrochemical Activates of the FeN-HNPC in Alkaline Electrolyte

The electrochemical activity for ORR was first evaluated using linear sweep voltammetry (LSV) curves in an alkaline solution.

© 2025 Wiley-VCH GmbH

As shown in **Figure 3**a, the FeN-HNPC exhibits the highest ORR activity with an onset potential (E_{onset}) of 1.15 V (vs RHE) and a half-wave potential ($E_{1/2}$) of 0.88 V, surpassing those of the FeN-NPC (E_{onset} = 0.97 V, $E_{1/2}$ = 0.76 V), HNPC (E_{onset} = 0.81 V, $E_{1/2}$ = 0.61 V), and Pt/C (E_{onset} = 1.03 V, $E_{1/2}$ = 0.85 V). Moreover, the FeN-HNPC catalyst demonstrates the smallest Tafel slope (93 mV dec^{-1}) and highest kinetic current density (J_k) of 18.75 mA cm^{-2} at 0.80 V compared with the control groups, implying faster ORR kinetics (Figure S15, Supporting Information). The superior ORR performance of the FeN-HNPC outperforms most nonprecious metal electrocatalysts (Table S4, Supporting Information). According to Equations (S13–S15), Supporting Information, the Koutecky–Levich (K–L) plots derived from rotating disk (RDE) measurements at various rotation speeds display good linearity at different potentials (Figure S16, Supporting Information), reflecting the first-order ORR kinetics.[31] According to the rotating ring disk electrode (RRDE) measurements and calculations by Equations (S16–S17), Supporting Information, the FeN-HNPC catalyst achieves an electron transfer number (n) of ≈4.0, with H_2O_2 yields below 5% (Figure S17, Supporting Information), confirming its efficient four-electron oxygen reduction mechanism.[32] Furthermore, the FeN-HNPC catalyst exhibits excellent ORR long-term durability, maintaining about 87% of its initial current density after 10 h in the chronoamperometry test, which is significantly higher than the commercial Pt/C catalyst (Figure S18, Supporting Information). Besides, the FeN-HNPC displays superior methanol tolerance compared to Pt/C (Figure S19, Supporting Information). The significant current drop observed for Pt/C likely stems from the competitive methanol oxidation on the Pt surface, which depletes active sites. In contrast, FeN-HNPC is inert toward methanol oxidation, maintaining high ORR selectivity and stability.[33]

In addition, in situ Raman spectroscopy was employed to monitor the formation of oxygen intermediates on the FeN-HNPC catalyst (Figure S20, Supporting Information). A new peak emerges at 450 cm^{-1}, with its intensity increasing as the potential decreases, indicating that the Fe-OH intermediates can be formed during ORR process and gradually accumulation at the Fe active sites.[34] Furthermore, the iodate (IO_3^-) reduction reaction (IO_3RR) performances of the different catalysts were performed in a mixed solution of 0.1 M KOH and saturated KIO_3 under a N_2 atmosphere. As displayed in Figure 3b, the LSV curve of the FeN-HNPC reveals a higher onset potential (0.90 V) than FeN-NPC (0.86 V) and HNPC (0.67 V). Additionally, the FeN-HNPC sample demonstrates the lowest Tafel slope of 257 mV dec^{-1} among all as-prepared samples, confirming its acceptable catalytic activity for IO_3RR and satisfactory kinetics (Figure S21, Supporting Information). Notably, the FeN-HNPC requires an IO_3RR potential of 0.28 V to achieve a current density of -5 mA cm^{-2}, while ORR needs 0.79 V under the same conditions, indicating that IO_3RR deviates more from its equilibrium potential under alkaline conditions and is consequently more challenging to activate.

The OER and IOR electrocatalytic activities were investigated in KOH and KOH/KI solutions, respectively. As shown in Figure 3c, the FeN-HNPC catalyst displays remarkable IOR activity with a low potential of 1.30 V at 10 mA cm^{-2}, lower than the FeN-NPC (1.38 V) and HNPC (1.46 V). For OER, the FeN-HNPC needs a potential of 1.80 V to reach 10 mA cm^{-2}, with a potential difference of 0.5 V compared to IOR. Such substantially lower oxidation potential suggests that IOR can reduce the charge voltage for battery, therefore improving energy efficiency. In addition, a smaller Tafel slope of the FeN-NHPC in IOR (72 mV dec^{-1}) than in OER (313 mV dec^{-1}) (Figure S22, Supporting Information) further confirms the superior kinetics for IOR. In situ digital microscope confirms the replacement of OER by IOR during the oxidation process on the FeN-HNPC in the presence of KI (Figure S23, Supporting Information). When oxidation at current density of 10 mA cm^{-2}, oxygen bubbles immediately generate on the cathode in the KI-free electrolyte, while no bubbles are observed in the KI-containing electrolyte. Moreover, the FeN-HNPC catalyst also demonstrates good stability for IOR over 80 h and a low potential of 1.62 V at 50 mA cm^{-2} (Figure S24a, Supporting Information), significantly outperforming OER (10 h and 2.89 V). After the OER test, the solution turns yellow (Figure S24b, Supporting Information), while it remains clear after the IOR test, likely due to carbon degradation by oxidation at the high OER potential.[35]

UV spectroscopy was employed to analyze the transformation of iodine species during IOR and IO_3RR processes in alkaline solutions. The oxidation process in KOH/KI solution illustrates that the absorption peak of I^-, located approximately at 225 nm, decreases while the peak for IO_3^- at near 290 nm increases, indicating the conversion of I^- to IO_3^- (Figure 3d,e).[36] Upon subsequent reduction, a slight increase in the I^- peak and a decrease in the IO_3^- peak are observed, suggesting the incomplete reduction of IO_3^- to I^-. The concentration of I^- steadily decreases, while IO_3^- gradually accumulates over multiple redox cycles in alkaline solution, which may negatively impact the lifespan of battery. Overlapping LSV curves in KOH with KIO_3 under O_2 atmospheres display higher current density compared to those under N_2 atmospheres, indicating the simultaneous reduction of oxygen and IO_3^- (Figure 3f). However, in the presence of excess IO_3^-, the half-wave potential of FeN-HNPC drops to 0.84 V, and the limiting current density also decreases, which can be detrimental to the discharge process of alkaline ZAIBs. Furthermore, IOR is unaffected by the gas atmosphere and demonstrates superior performance compared to OER. These results lead to a low potential gap of 0.42 V between ORR and IOR in alkaline media, which is significantly smaller than the gap of 0.92 V between ORR and OER. This finding highlights the strong optimization effect of KI on the charge process.

To investigate the charge and discharge behaviors, alkaline ZAIBs and ZABs were assembled by employing the as-prepared catalysts as the air cathodes, as the configuration shown in Figure S25 (Supporting Information). As demonstrated in Figure 3g; and Figure S26a (Supporting Information), the FeN-HNPC-based alkaline ZAIBs exhibit the narrowest voltage gap of 0.74 V at 10 mA cm^{-2}, outperforming FeN-NPC (0.82 V), HNPC (1.20 V), and significantly surpassing conventional ZABs. This trend persists across current densities from 1 to 20 mA cm^{-2}, confirming the inherent advantage of ZAIB configuration in suppressing polarization. Additionally, the FeN-HNPC, FeN-NPC and HNPC-based alkaline ZAIBs achieve peak power densities of 141.8, 59.8, and 55.8 mW cm^{-2}, respectively (Figure S26b,c, Supporting Information), exceeding their ZAB counterparts (127.3, 53.4, and 51.6 mW cm^{-2}). Furthermore, the FeN-HNPC-based alkaline ZAIB displays a specific capacity of 792.6 mAh g_{zn}^{-1} at 10 mA cm^{-2} based on the consumed mass of Zn

© 2025 Wiley-VCH GmbH

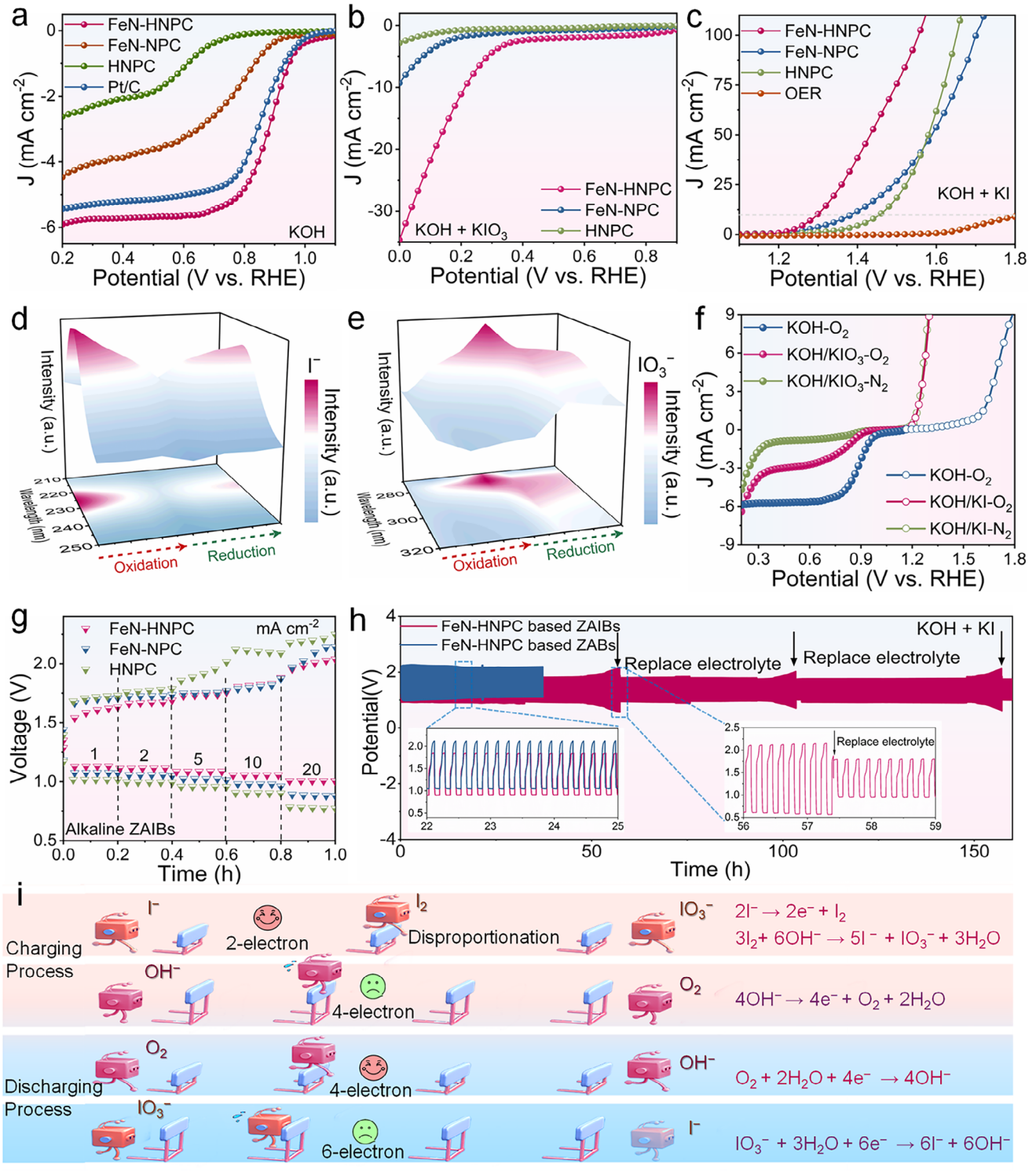

Figure 3. Electrochemical performances of the different catalysts in alkaline electrolytes. a) ORR LSV curves (1600 rpm) of the FeN-HNPC, FeN-NPC, HNPC, and 20% Pt/C catalysts in 0.1 M KOH solution. LSV curves for b) IO_3RR under 0.1 M KOH with saturated KIO_3 solution and c) IOR under 1.0 M KOH with 1.0 M KI solution. UV spectra changes of characteristic substances of d) I^- and e) IO_3^- in KOH/KI solution during oxidation and reduction processes. f) Overlapping LSV curves of the FeN-HNPC in O_2 or N_2 saturated alkaline electrolytes. g) Charge and discharge polarization plots at different current densities of alkaline ZAIBs (KOH/KI) with the FeN-HNPC, FeN-NPC, and HNPC air electrodes. h) Galvanostatic discharge/charge cycling curves of FeN-HNPC-based alkaline ZABs and ZAIBs at 10 mA cm^{-2}. i) Schematic reaction diagrams of charge and discharge processes at alkaline ZABs and ZAIBs.

© 2025 Wiley-VCH GmbH

anode (Figure S26d and Equation (S18), Supporting Information), which is comparable to the conventional alkaline ZABs (766.3 mAh g_{zn}^{-1}). At a constant current density of 10 mA cm^{-2}, the FeN-HNPC-based ZAIB exhibits a discharge voltage of 1.05 V and a charge voltage of 1.79 V, corresponding to a voltage gap of 0.74 V (Figure 3h). However, after only 50 h of operation, a noticeable increase in voltage gap is observed for the FeN-HNPC electrode, while the FeN-NPC and HNPC counterparts exhibit degradation after 45 and 30 h, respectively (Figure S26e,f, Supporting Information). The rapid decline in electrochemical performances of ZAIBs is primarily attributed to the fact that irreversible disproportionation of I_2 causes accumulation of IO_3^- in alkaline solution (Figure 3i). The generated IO_3^- is difficult to be completely reduced during discharge due to the complex 6-electron reaction. Although the electrochemical performances of ZAIBs can be virtually restored by replacing the electrolyte, the repeated operation brings additional complexity.

2.4. Electrochemical Performances of the FeN-HNPC in Neutral Electrolyte

The ORR activity of the FeN-HNPC in 0.1 M PBS (**Figure 4a**) shows an onset potential (E_{onset}) of 0.93 V and a half-wave potential ($E_{1/2}$) of 0.79 V, outperforming the as-prepared FeN-NPC (0.80 and 0.43 V), HNPC (0.52 and 0.31 V) catalysts, and the commercial Pt/C (0.92 and 0.74 V). Tafel slopes were further calculated to evaluate the ORR kinetics on the as-prepared catalysts.[37] Compared with that of the FeN-NPC (323 mV dec^{-1}), HNPC (348 mV dec^{-1}), and Pt/C (149 mV dec^{-1}), the FeN-HNPC sample displays the smallest Tafel slope value (101 mV dec^{-1}), implying its faster ORR kinetic process (Figure S27a, Supporting Information). Furthermore, the FeN-HNPC achieves a considerable J_k of 14.3 mA cm^{-2} at 0.7 V in neutral media (Figure S27b, Supporting Information), which is superior to commercial Pt/C (6.0 mA cm^{-2}). Moreover, the FeN-HNPC shows superior ORR performance compared to specially developed electrocatalysts under neutral conditions (Table S5, Supporting Information). Its substantial specific surface area promotes the formation of numerous transporting channels and increases the exposure of active sites, making it highly effective for electrocatalytic reactions.[38] From the results of electrochemical impedance spectroscopy (EIS), the FeN-HNPC delivers the lowest charge transfer resistance (398.9 Ω), in comparison to the Pt/C (1215.2 Ω) and FeN-NPC (3453.8 Ω) (Figure S28, Supporting Information). Concurrently, the calculated electrochemical double-layer capacitance (C_{dl}) for the FeN-HNPC is 5.89 mF cm^{-2} (Figure S29, Supporting Information), which is larger than that of the FeN-NPC (4.84 mF cm^{-2}) and HNPC (2.48 mF cm^{-2}), thus further substantiating the superiority of the FeN-HNPC material. In addition, the K–L plots and RRDE measurements according to Equations (S13–S17), Supporting Information verify the 4-electron ORR pathway, with H_2O_2 yield of 6.7% for the FeN-HNPC in neutral conditions (Figures S30 and S31, Supporting Information). The excellent stability of the FeN-HNPC in ORR is evidenced by a minimal decrease in current density after 10 h (Figure S32, Supporting Information).

The IRR performances of the as-prepared electrocatalysts were explored in 0.1 M PBS containing 10 mM I_2 under the N_2 atmosphere.[39] As displayed in Figure 4b, the IRR polarization curves of the FeN-HNPC, FeN-NPC, and HNPC indicate distinct reduction peaks, where the FeN-HNPC catalyst shows the most favorable peak potential (0.85 V) and the highest peak reduction current density (11.64 mA cm^{-2}). Additionally, the FeN-HNPC exhibits the smallest Tafel slopes for IRR (74 mV dec^{-1}), in comparison to other catalysts (Figure S33a, Supporting Information). Interestingly, IRR requires just 0.98 V to reach a current density of -2 mA cm^{-2} under neutral electrolyte, whereas ORR needs 0.78 V to the same current density, indicating the kinetics and thermodynamics of IRR in neutral media are more favorable than those of ORR. These outcomes contrast with the reduction behavior of IO_3^- in alkaline conditions.

The IOR activities of the different electrocatalysts were further investigated in 1.0 M PBS with 1.0 M KI. As shown in Figure 4c, the FeN-HNPC exhibits a smaller IOR potential of 1.15 V to reach 50 mA cm^{-2}, lower than those of the FeN-NPC (1.19 V) and HNPC (1.21 V). In the absence of KI, the FeN-HNPC requires a higher potential of 2.39 V to achieve 10 mA cm^{-2} for OER. The Tafel slope of the FeN-HNPC for IOR is 25 mV dec^{-1} (Figure S33b, Supporting Information), significantly smaller than that of OER (355 mV dec^{-1}). In addition, the FeN-HNPC displays stable IOR performance over 100 h without significant voltage drop, far surpassing OER stability (10 h) (Figure S34a, Supporting Information). As the IOR continues, it can be observed that a yellow hue around the electrode without any bubbles, suggesting that I^- is preferentially consumed over H_2O under neutral electrolyte (Figure S34b, Supporting Information). After running the IOR for 150 h, no detectable I^- remains in the solution and bubbles forms on the electrode, suggesting that nearly-complete conversion of I^- to I_3^-, as well as the participation of H_2O to O_2 (Figure S34c, Supporting Information). The superimposed LSV curves in the neutral condition (Figure 4d) show that the IRR and IOR occur preferentially, with a potential gap of 0.13 V (E_{J5}-E_{10}), which is significantly smaller than that of the OER-ORR pair (1.51 V for $E_{1/2}$-E_{10}), indicating that the introduction of KI into the neutral electrolyte can simultaneously boost the charge/discharge performance. UV spectrophotometry was further employed to observe the characteristic peaks in 1.0 M PBS with 1.0 M KI solution for monitoring the changes in iodine species. As shown in Figure 4e,f, the I^- peak around 225 nm gradually decreases with the increase of oxidation time, while the I_3^- peaks centered at 280 and 360 nm increase. The opposite occurs during the reduction process.[40] These insights corroborate the reversibility of the I^-/I_3^- redox reaction in neutral electrolytes, supporting the long-cycle capability of neutral ZAIBs.

For proof of concept, neutral liquid ZAIBs were assembled using 1.0 M $Zn(OAc)_2$ containing 1.0 M KI. Cyclic voltammetry (CV) analysis reveals that, compared to neutral conventional ZABs (Figure 4g), the neutral ZAIBs exhibit stronger ORR peaks and distinct IRR/IOR redox features in the voltage range of 1.0–1.3 V.[41] Interestingly, the pronounced I_3^- reduction peak in a neutral liquid is sharply contrasted with the weaker IO_3^- reduction peak in alkaline electrolyte (Figure S35, Supporting Information), indicating the facilitative role of iodine species in oxygen electrocatalysis. The charge and discharge performance of the neutral batteries based on various catalysts was then studied across a range of current densities (from 1 to 20 mA cm^{-2}, Figure 4h; and Figure S36a, Supporting Information). The

© 2025 Wiley-VCH GmbH

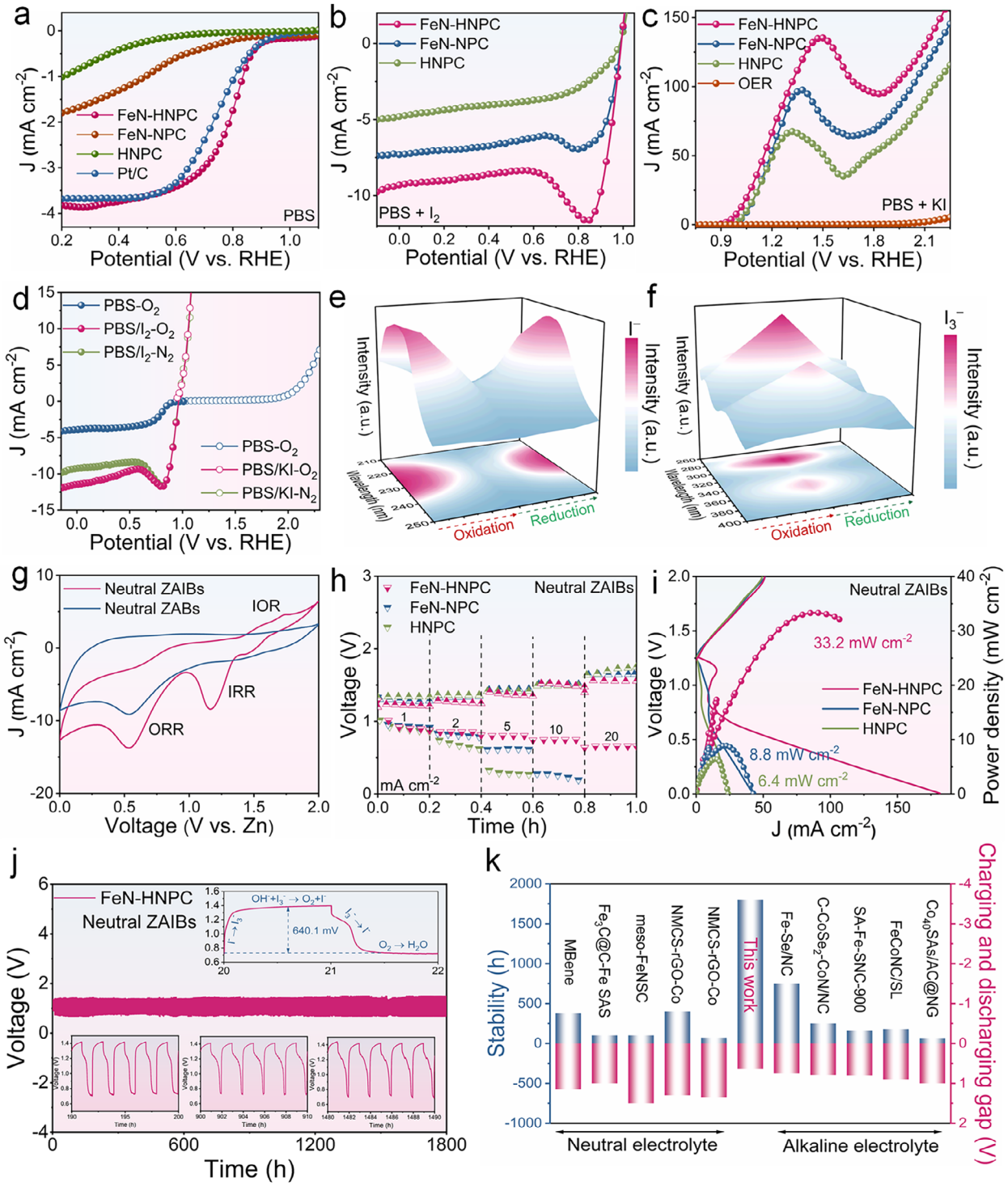

Figure 4. Electrochemical performances of the different catalysts in neutral electrolytes. a) ORR LSV curves (1600 rpm) of the FeN-HNPC, FeN-NPC, HNPC, and 20% Pt/C catalysts in 0.1 M PBS. LSV curves for b) IRR under 0.1 M PBS with 10 mM I_2 electrolyte and c) IOR under 1.0 M PBS with 1.0 M KI electrolyte. d) Overlapping LSV curves of FeN-HNPC in O_2 or N_2 saturated neutral electrolytes. UV spectra changes of characteristic substances of e) I^- and f) I_3^- in PBS/KI solution during oxidation and reduction processes. g) CV curves of the FeN-HNPC-based neutral ZABs with $Zn(OAc)_2$ and FeN-HNPC-based neutral ZAIBs with $Zn(OAc)_2$/KI. h) Charge and discharge polarization plots at different current densities for neutral ZAIBs using FeN-HNPC, FeN-NPC, and HNPC as air electrodes. i) Charge and discharge polarization curves and corresponding power density curves for neutral ZAIBs using FeN-HNPC, FeN-NPC, and HNPC as air electrodes. j) Galvanostatic discharge/charge cycling curves at 2 mA cm^{-2} of neutral ZAIBs with the FeN-HNPC air electrodes (charge for 1 h and discharge for 1 h). k) Comparison of cycling performance and charge/discharge gap of neutral ZAIBs using FeN-HNPC with other reported catalysts in alkaline and neutral batteries.

© 2025 Wiley-VCH GmbH

FeN-HNPC-based neutral ZAIBs exhibit the lowest charge voltage (1.22 V) at 1 mA cm^{-2} compared with the FeN-NPC (1.27 V) and HNPC (1.34 V), while all significantly surpass conventional ZABs. Under a discharge current density of 5 mA cm^{-2}, neutral ZAIBs based on FeN-HNPC maintain a voltage of 0.75 V, exceeding FeN-NPC (0.57 V), HNPC (0.28 V), and conventional ZABs, confirming that the introduction of I^- promotes ORR kinetics. DFT calculations (Figure 1b) have demonstrated that I^- can form strong bonds with Fe on the surface of FeN-HNPC, and recent studies have reported that the interaction between I^- and the catalyst surface can lower the energy barrier for the ORR to enhance reaction kinetics.[10] Moreover, the FeN-HNPC-based neutral ZAIB achieves a peak power density of 33.2 mW cm^{-2}, far exceeding FeN-NPC (8.8 mW cm^{-2}), HNPC (6.4 mW cm^{-2}) (Figure 4i), and doubling the performance of neutral ZAB counterparts (Figure S36b, Supporting Information). The observed fluctuations in the power density curves are mainly caused by the kinetic inconsistency between the ORR and IRR processes.[42] Furthermore, FeN-HNPC-based neutral ZAIB maintains a stable discharge voltage of 0.73 V at 5 mA cm^{-2}, along with a specific capacity of 650.0 mAh g_{zn}^{-1} and an energy density of 474.5 Wh kg_{zn}^{-1} (Figure S37, Supporting Information), which is considerably higher than those of conventional ZABs (0.71 V, 428.6 mAh g_{zn}^{-1} and 304.3 Wh kg_{zn}^{-1}). Long-term cycling at 2 mA cm^{-2} demonstrates that the FeN-HNPC-based neutral ZAIBs showcase a lifespan of 1800 h (2 h per cycle) without electrolyte replacement (Figure 4j), considerably superior to FeN-NPC (162 h) and HNPC (52 h) (Figure S38, Supporting Information). In stark contrast, all tested conventional ZABs degrade rapidly within 80 h due to the adverse effects of higher charging voltage (Figure S36c, Supporting Information). Postcycling characterizations (Figure S39, Supporting Information) confirm structural robustness and compositional integrity of the FeN-HNPC catalyst.[43] The FeN-HNPC-based neutral ZAIBs also exhibit a reduced voltage gap of 640.1 mV and a higher energy efficiency of 54.0%, outperforming both FeN-NPC (823.1 mV, 40.2%) and HNPC (978.4 mV, 32.6%), as well as conventional ZABs. The enhanced energy efficiency may be attributed to the well-balanced multifunctional catalytic activity of FeN-HNPC, which effectively lowers polarization and minimizes voltage losses during charge–discharge processes. As summarized in Figure 4k; and Table S6 (Supporting Information), the FeN-HNPC-based neutral ZAIB surpasses most previously reported neutral and alkaline ZABs in critical metrics, particularly in cycling stability and voltage gap. Remarkably, the performance of neutral ZAIB is comparable to or even exceeds that of other zinc–air hybrid batteries (Table S7, Supporting Information).

2.5. Understanding the Mechanism of Neutral ZAIBs

To systematically investigate the reaction mechanisms of neutral ZAIBs, a series of characterizations, including in situ Raman spectroscopy and ex situ XRD, were performed during charge and discharge processes. The characteristic Raman peaks of I_3^- situated at ≈105–115 cm^{-1} and I_5^- found around ≈165–175 cm^{-1} demonstrate an increase with charge and a reverse trend with discharge, confirming the reversible conversion between I^- and I_3^- in the neutral electrolyte (**Figure 5a**). The peak intensity of I_5^- is lower than that of I_3^-, which can be attributed to the reversible conversion of I_3^- to I_5^-. To further explore the electron-transfer number during IRR process, rotating disk electrode measurements were conducted at rotation rates of 900, 1225, 1600, 2025, and 2500 rpm (Figure 5b). The relationship between the rotation speed and current is derived from Figure 5c. Calculated with the K–L equation, the electron-transfer number for the reduction of iodine species in ZAIBs is 0.624, demonstrating the fast conversion mechanism between I_3^- and I^-.[44] Figure 5d exhibits XRD patterns of the cathode in fully charged and discharged states in neutral ZAIBs. In the fully discharged state, diffraction peaks of $Zn_5(OH)_8(CH_3CO_2)_2{\cdot}2H_2O$ (ZHA) can be observed, which is due to the reaction between $Zn(OAc)_2$ and OH^- ions produced from the ORR at the air cathode.[45] Optical photographs of the air cathode postdischarge show a significant accumulation of white substance (Figure S40, Supporting Information). These results further confirm the formation of ZHA, consistent with discharged products reported in neutral ZABs with $Zn(OAc)_2$ electrolyte.[13,14]

The formation of insoluble and low-conductivity ZHA can hinder the performance by obstructing mass transport pathways and active sites, as confirmed by EIS, which shows a slight increase in R_{ct} following ZHA formation. Notably, the FeN-HNPC cathode exhibits a relatively minor R_{ct} increase from 56.7 to 295.9 Ω, whereas the FeN-NPC cathode experiences a substantially larger increase from 98.1 to 383.6 Ω (Figure S41, Supporting Information), suggesting the hierarchical porous architecture of FeN-HNPC effectively mitigates ZHA-induced resistance growth. Complementary SEM analysis further elucidates the morphological differences between the two cathodes upon ZHA formation. The continuous ZHA flakes accumulate on the FeN-NPC surface (Figure S42, Supporting Information), forming a dense layer that fully covers the catalyst surface. In contrast, the FeN-HNPC confines ZHA deposition within its macropores, preventing complete surface coverage and preserving ion and O_2 diffusion pathways. This result clearly demonstrates that the ZHA precipitates can be spatially confined within a hierarchical mesoporous–macroporous honeycomb architecture, and the resulting structural advantage preserves open pathways for gas diffusion, thereby facilitating sustained electrochemical reactions and mitigating mass transport limitations.

The cathode-side reactions in the neutral ZAIBs system during discharge are as follows (Equations (1–4)

Air Cathode (Discharge process)

$$I_5^- \rightleftharpoons I_3^- + I_2 \tag{1}$$

$$I_3^- + 2e^- \rightarrow 3I^- \tag{2}$$

$$O_2 + 2H_2O + 4e^- \rightarrow 4OH^- \tag{3}$$

$$\frac{5}{2}\,Zn^{2+} + 4OH^- + CH_3COO^- + H_2O \rightarrow \frac{1}{2}\,Zn_5\,(OH)_8\,(CH_3CO_2)_2 \cdot 2H_2O \tag{4}$$

In the fully charged state, the disappearance of ZHA diffraction peaks indicates its complete decomposition. The reversible

© 2025 Wiley-VCH GmbH

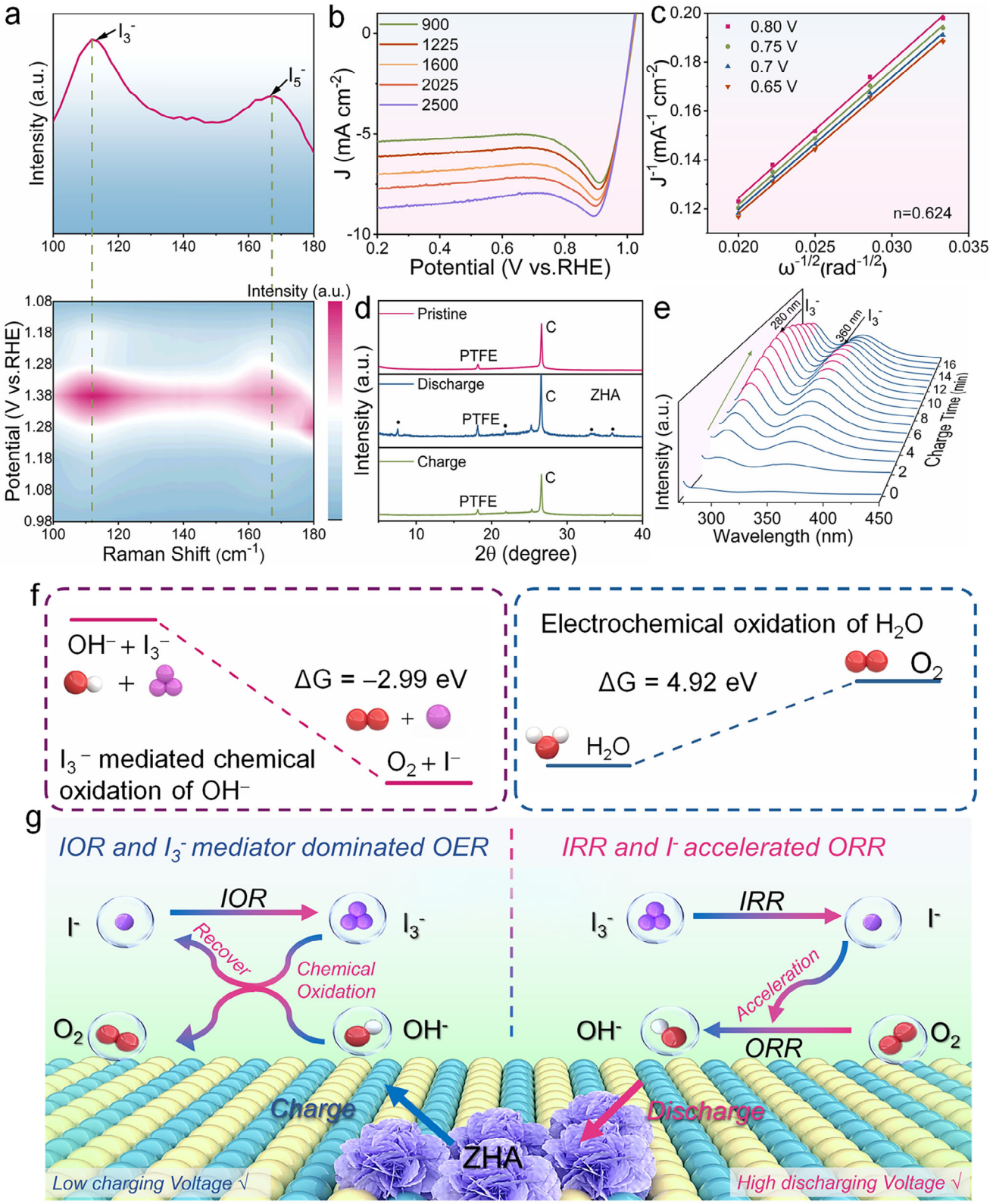

Figure 5. Charge and discharge mechanism of the neutral ZAIBs. a) In situ Raman spectra of $Zn(OAc)_2$/KI solution at neutral ZAIBs on different charge/discharge time. b) LSV curves of FeN-HNPC for the IRR at different rotation rates. c) The fitted curve of rotation rate and current in the panel. d) The corresponding XRD patterns of air cathodes obtained from neutral ZAIBs after discharge and charge processes. e) In situ UV spectra of $Zn(OAc)_2$/KI solution at neutral ZAIBs for different charge time. f) The reaction energy ΔG of each oxidation process in $Zn(OAc)_2$/KI and $Zn(OAc)_2$. g) Schematic illustration of cycle mechanism of neutral ZAIBs.

© 2025 Wiley-VCH GmbH

transformation of ZHA is further corroborated by FTIR spectroscopy performed on air cathode at different charge and discharge stages (Figure S43, Supporting Information). The FTIR spectra reveal three characteristic peaks of ZHA, of which the peaks at 1567 and 1415 cm^{-1} corresponding to the vibration modes of carboxylate (COO^-) group, while the strong peaks in the range of 600–1000 cm^{-1} range can be attributed to the δ-mode vibration of Zn—OH bonds.[46] In the discharge progresses, the intensities of the COO^- and Zn—OH peaks gradually increase, indicating the continuous accumulation of ZHA on the catalyst surface, which further confirms its role as the primary discharge product. Upon charging, these peaks diminish significantly and eventually disappear, demonstrating the effective decomposition of ZHA. This spectral evidence strongly supports the reversible formation and decomposition of ZHA, highlighting its dynamic participation in the charge–discharge cycle of the neutral ZAIBs system.

To further substantiate the charge mechanism, in situ UV testing was used to validate the change of iodine-containing redox mediators. Neutral ZAIBs are first discharged at 2 mA cm^{-2} to form ZHA at the air cathode, followed by constant-current charge. As shown in Figure 5e, the in situ UV spectra reveal an initial increase in I_3^- concentration, followed by a gradual decline as charging proceeds. The initial I_3^- accumulation results from the oxidation of I^- to I_3^- and I_5^- (Equations (5) and (6)). However, as ZHA decomposes under charging voltage (Equation (7)), the released OH^- spontaneously reacts with the accumulated I_3^- (Equation (8)), leading to its gradual depletion via a chemical oxidative process.[47] DFT calculations show that the chemical oxidative of OH^- by I_3^- to form O_2 and H_2O delivers a free energy of -2.99 eV (Figure 5f), whereas electrochemical oxidation of OH^- requires 4.92 eV.[10] To quantitatively evaluate the oxygen evolution during charging, a Swagelok battery was assembled using FeN-HNPC (Figure S44, Supporting information). The calculated electron-transfer number is ≈3.76 per mole of oxygen generated, closely matching the theoretical value of 4 electrons. This result provides strong evidence for the occurrence of the oxygen evolution at the air cathode during the charging process.[48]

Air Cathode (Charge process)

$$3I^- - 2e^- \rightarrow I_3^- \quad (5)$$

$$I_3^- + I_2 \rightleftharpoons I_5^- \quad (6)$$

$$\frac{1}{2}\,Zn_5\,(OH)_8\,(CH_3CO_2)_2 \cdot 2H_2O \rightarrow 2H_2O + \frac{5}{2}\,Zn^{2+} + CH_3COO^- + 4OH^- \quad (7)$$

$$4OH^- + 2I_3^- \rightarrow O_2 + 2H_2O + 6I^- \quad (8)$$

Adsorption experiments (Figure S45, Supporting Information) demonstrate that FeN nanoparticles within the catalyst framework selectively interact with and adsorb polyiodine species, thereby stabilizing iodide redox dynamics. To investigate the role of I_3^- in ZHA decomposition, the ZHA-loaded FeN-HNPC electrode was charged at 1.3 V for 500 s in two different electrolytes (Figure S46, Supporting Information). In pure $Zn(OAc)_2$ electrolyte, white ZHA residues persist on the electrode surface, whereas in I_3^--containing $Zn(OAc)_2$ electrolyte, ZHA is nearly fully decomposed, demonstrating the significant promotion of ZHA decomposition through a spontaneous reaction involving the consumption of OH^-.

As illustrated in Figure 5g, the neutral ZAIBs operate through reversible iodide-oxygen coupled redox mechanisms. During discharge, I_3^- is preferentially reduced to I^-, followed by ORR to generate OH^-, which reacts with $Zn(OAc)_2$ to produce ZHA. The real-time pH monitoring (Figure S47, Supporting Information) reveals an initial sharp rise (OH^- accumulation) followed by a gradual decline (ZHA precipitation), consistent with this pathway. The FeN-HNPC catalyst synergistically facilitates IRR and ORR kinetics, elevating discharge voltage. During charging, I^- is oxidized back to I_3^-, while ZHA decomposes to release OH^-. The released OH^- reacts with I_3^-, triggering spontaneous chemical oxidation that regenerates I^- and produces O_2. Concurrently, pH dynamics shift from a slow rise at the beginning of the process, and then drop rapidly due to the consumption of OH^-. The FeN-HNPC catalyst significantly accelerates iodine-mediated oxidation process, replacing the high-overpotential OER, reducing the charging voltage and boosting the energy efficiency of battery. The synergistic interplay of reversible I^-/I_3^- and OH^-/O_2 redox couples, coupled with the dynamic equilibrium of ZHA precipitation/decomposition throughout the reaction process, collectively enhances the long-term cycling stability of the neutral ZAIBs.

To fully understand the effects of $Zn(OAc)_2$/KI solution in neutral ZAIBs on stabilizing the zinc anode, a comprehensive evaluation of related tests was performed to investigate the stripping and deposition mechanism of the zinc anode. As shown in **Figure 6a**, the XRD patterns of cycled zinc anodes in both neutral ZAIBs and ZABs reveal a new diffraction signal regarding the ZHA. Previous works have reported that the excess OH^- produced at the air cathode would migrate into the anode and react with Zn^{2+} to form ZHA at the Zn surface.[14] Impressively, the Zn anode with $Zn(OAc)_2$ electrolyte exhibits the sharp and strong peaks of ZHA after cycling in neutral ZABs. On the contrary, considerably weaker intensities of ZHA in the anode are observed with $Zn(OAc)_2$/KI electrolyte, indicating more efficient reversible stripping and deposition of Zn^{2+} in neutral ZAIBs. The corresponding SEM images display that the zinc foil after cycling in KI-containing neutral electrolyte maintains a compact and uniform surface without dendrites (Figure S48, Supporting Information). In contrast, massive dendrites and ZHA flakes appear on the Zn surface after cycling in $Zn(OAc)_2$ electrolyte. A similar morphological difference can also be observed in laser scanning confocal microscopy (LSCM). The corresponding 3D images reveal large humps and aggregates with a maximum height of more than 50 µm for the cycled Zn anode in $Zn(OAc)_2$ (Figure 6b), whereas, the surface of Zn anode in $Zn(OAc)_2$/KI presents a smooth surface with a lower altitude intercept of 15 µm (Figure 6c).[49] The above results further demonstrate that the introduction of iodine species promotes the reversibility of Zn electrodeposition/stripping in neutral electrolytes. The reactions of the zinc anode in neutral ZAIBs can be expressed as follows (Equations (9) and (10))[14]

© 2025 Wiley-VCH GmbH

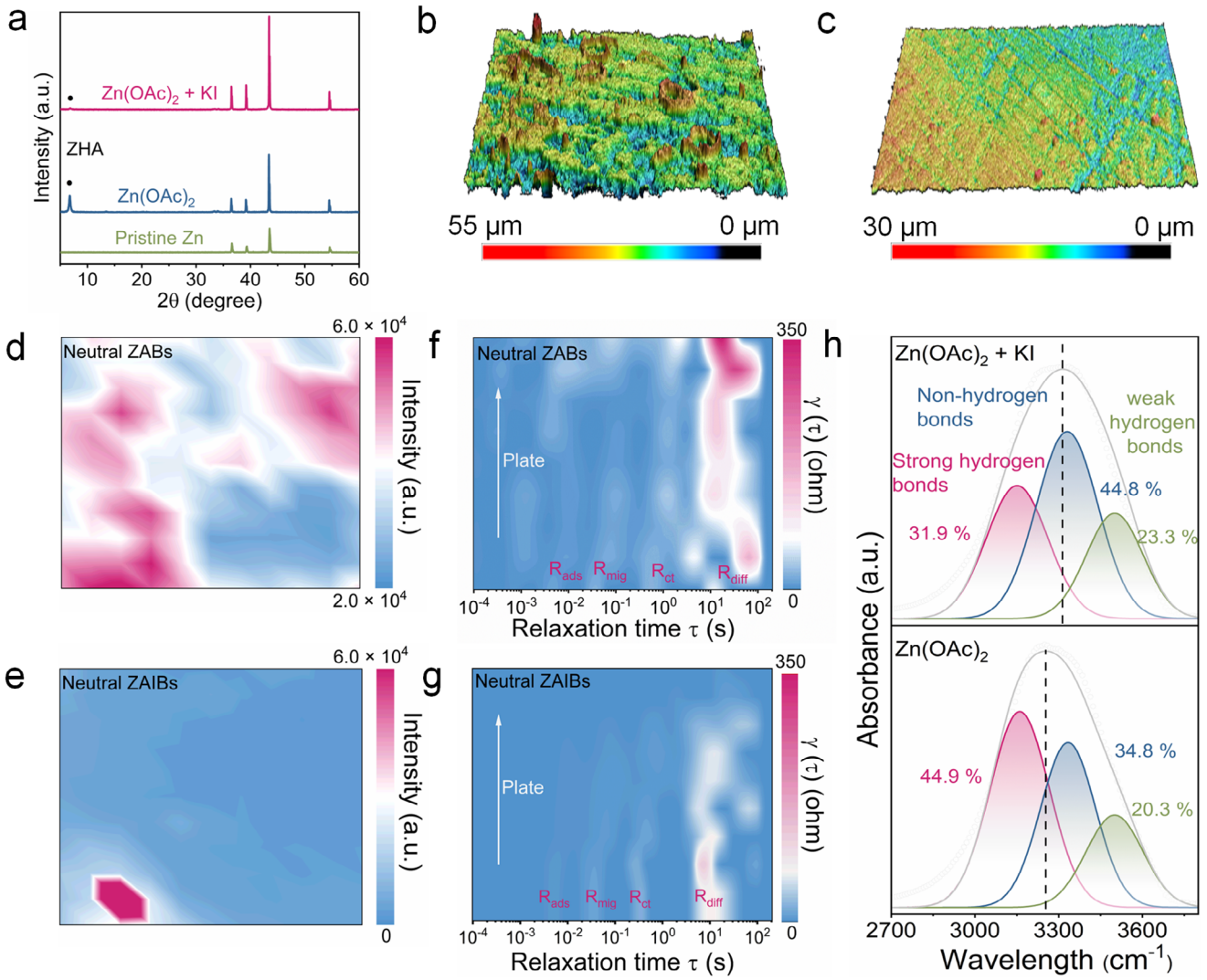

Figure 6. Effects of different neutral electrolyte on zinc anode. a) XRD patterns of zinc anodes after 100 cycles in different neutral electrolytes. Laser scanning confocal microscope 3D topography images of zinc anodes after 100 cycles in b) $Zn(OAc)_2$ and c) $Zn(OAc)_2$/KI electrolytes. Raman mapping of 10 μm-zinc anodes in d) neutral ZABs and e) ZAIBs after 100 cycles. The analysis of distribution of DRT of operando EIS during zinc deposition in f) neutral ZABs and g) ZAIBs after 100 cycles. h) Fitted FTIR spectra of $Zn(OAc)_2$/KI and $Zn(OAc)_2$ electrolytes.

Zn Anode (Discharge process)

$$4Zn + 2O_2 + Zn^{2+}(CH_3CO_2)_2^- + 6H_2O \rightarrow Zn_5(OH)_8(CH_3CO_2)_2 \cdot 2H_2O \quad (9)$$

Zn Anode (Charge process)

$$Zn_5(OH)_8(CH_3CO_2)_2 \cdot 2H_2O \rightarrow 4Zn + 2O_2 + Zn^{2+}(2CH_3CO_2)_2^- + 6H_2O \quad (10)$$

Raman mapping (collected at 750 cm^{-1}, CH_3COO^- signal) can visualize the 2D distribution of the ZHA products. Clearly, the cycled zinc anode in neutral ZABs is covered with large amounts of ZHA (Figure 6d), while less accumulation of ZHA can be observed in neutral ZAIBs (Figure 6e). The interfacial kinetics is an essential indicator to monitor the dynamics of the Zn^{2+} transport, as investigated by in situ EIS and distribution of relaxation time (DRT) (Figure S49, Supporting Information). The relaxation times (τ) at the scales of 10^{-2}, 10^{-1}, 10^{0}, and 10^{1} are assigned to the Zn^{2+} adsorption (R_{ads}), surface migration (R_{mig}), charge transfer (R_{ct}), and diffusion (R_{diff}) processes, respectively (Figure 6f,g). Here, the increases in τ represent hindered interfacial kinetics due to the large amounts of ZHA on the surface. Notable changes in R_{mig}, R_{ct}, and R_{diff} highlight the significant ZHA flakes accumulation on zinc foil in ZABs, which affects Zn deposition and leads to dendrite formation. During the Zn plating process, all the τ values in ZAIBs are much smaller compared to those in ZABs, suggesting that the introduction of iodide species can significantly accelerate the interfacial reaction kinetics.

The understanding of the interactions occurring within the electrolyte is essential for elucidating the underlying mechanisms responsible for the enhanced performance observed in neutral ZAIBs. Fourier transform infrared (FTIR) spectroscopy

© 2025 Wiley-VCH GmbH

reveals that the addition of KI in $Zn(OAc)_2$ solution leads to a blue shift in the O–H stretching vibration (2800–3600 cm^{-1}) (Figure 6h), indicating the replacement of Zn^{2+}–H_2O coordination by Zn^{2+}–I.[50] Moreover, the O–H signal can be divided into three characteristic peaks: strong hydrogen bonds, nonhydrogen bonds, and weak hydrogen bonds. The percentage of strong hydrogen bonds exhibits a downward trend while nonhydrogen bonds demonstrate an increase in the $Zn(OAc)_2$/KI system. These results verify that H_2O molecules are effectively bound in the $Zn(OAc)_2$/KI electrolyte due to the reconstruction of the hydrogen bond network, thereby inhibiting the hydrogen evolution reaction (HER).[51] The LSV measurements further demonstrate a higher HER overpotential value in the $Zn(OAc)_2$/KI compared to the pure $Zn(OAc)_2$, indicating its inhibitory effect on the side reaction after the introduction of KI (Figure S50, Supporting Information), in agreement with the FTIR results. Anticorrosion capabilities are essential for the long-term utilization of zinc anodes. Following the extrapolation of the Tafel line on linear polarization curves (Figure S51, Supporting Information), a higher corrosion potential of −0.027 V and a smaller corrosion current density value of 8.98×10^{-4} A cm^{-2} are obtained for the zinc anode in the $Zn(OAc)_2$/KI electrolyte in comparison to the $Zn(OAc)_2$ electrolyte (−0.036 V and 1.04×10^{-3} A cm^{-2}.), reflecting a significantly decreased tendency toward corrosive reactions through the involvement of KI.[52] Moreover, the high solubility of KI in $Zn(OAc)_2$ solutions yields a higher concentration of conductive iodide-containing ions, resulting in elevated ionic conductivity (56.23 mS cm^{-1}) and Zn^{2+} transference number (0.62) for the $Zn(OAc)_2$/KI electrolyte compared to 29.50 mS cm^{-1} and 0.37 for the $Zn(OAc)_2$ electrolyte (Figure S52, Supporting Information). The above results verify that the addition of KI in the neutral electrolyte enables synchronous regulation, which includes fast ionic conductivity coupled with high hydrogen evolution barriers and inhibition of dendrites formation, ultimately enhancing the performance of neutral ZAIBs.

2.6. Advantages of the Neutral ZAIBs

To simulate charging demands in practical applications while ensuring discharge stability, neutral ZAIBs were subjected to rapidly charged at 10 mA cm^{-2} for 6 min, followed by discharged at 1 mA cm^{-2} for 60 min.[53] Under these conditions, the neutral ZAIBs demonstrate a small ΔE of 0.59 V and a high round-trip energy efficiency of 57.9% (**Figure 7a**). After 200 h of operation, the ΔE increases by only 0.1 V, and energy efficiency slightly declined to 52.1%. Even after 320 h of fast charging, the neutral ZAIBs continue to function effectively. To further assess the performance under constrained electrolyte conditions, a coin-type ZAIB with an electrolyte volume limited to 80 µL was operated at a current density of 2 A g^{-1} (Figure 7b).[54] The results show stable operation for over 100 h (≈300 cycles) with negligible capacity decay, underscoring the robustness of the battery in electrolyte-limited environments. Additionally, a pouch cell configuration was employed, featuring a streamlined packaging design with an electrode area of 25 cm^2 and total battery mass of 10.1 g (Figure 7c).[55] This configuration enables stable cycling for 120 h at 1 mA cm^{-2} (Figure 7d) and delivers a specific capacity of 775.2 mAh g_{zn}^{-1} at 5 mA cm^{-2} (Figure S53, Supporting Information). Energy density calculations for pouch cell accounting for all active and inactive components reveal competitive metrics of 183.4 Wh kg^{-1} (gravimetric) and 41.27 Wh L^{-1} (volumetric) (Figure 7e), demonstrating the practical potential of the neutral ZAIB system.

To investigate the stability and performance of cathode materials, the impact of reduced charge voltage on the cathode material of the ZAIBs under neutral conditions was investigated by Raman and XPS analysis. As shown in Figure 7f, the Raman peaks at 1338.7 and 1583.5 cm^{-1} are indicative of sp^2-type carbon, while those at 1229.0 and 1475.7 cm^{-1} correspond to sp^3-type carbon.[56] The area ratio of sp^3/sp^2 exhibits a decline from 60.0% to 40.0% after cycling in $Zn(OAc)_2$ solution, which is due to the corrosion effects by high-potential of OER.[57] However, in $Zn(OAc)_2$/KI solution, this ratio remains nearly unchanged, indicating that the reduced charge voltage lowers the oxidation tendency of the electrocatalyst, thereby preventing the oxidation of sp^3-disordered carbon. Moreover, the analysis of C 1s XPS spectra provides additional evidence for the protective effect of lower voltage on the catalyst (Figure S54, Supporting Information). Following the cycling of neutral ZABs, a new C═O peak appears at 288.9 eV, accompanied by a notable sharpening and intensification of the broad C—O peak, indicative of a pronounced degree of carbon corrosion (oxidation). In contrast, the intensity changes of the C═O and C—O peaks are found to be weaker after cycling in neutral ZAIBs, demonstrating that the surface carbon of the cathode is effectively protected. These findings are in accordance with the Raman results. Further atomic ratio analysis is presented in Figure 7g, where the O atomic ratio and the content of C—O and C═O bonds significantly increase after cycling in $Zn(OAc)_2$ solution. These results contrasted with the changes observed in the presence of KI.

Furthermore, even at a high current of 100 mA, FeN-HNPC exhibits stable cycling performance (Figure S55a, Supporting Information). Postcycling SEM images (Figure S55b, Supporting Information) reveal that the honeycomb porous carbon structure of FeN-HNPC remains intact without aggregation or collapse. XPS analysis (Figure S55c, Supporting Information) confirms that negligible changes in the Fe 2p binding energy, indicating that the local chemical environment of Fe active sites remains unchanged after cycling. These findings collectively demonstrate that the reversible iodide-oxygen redox reactions in neutral ZAIBs play a crucial role in mitigating catalyst oxidation, thereby significantly enhancing the long-term cycling stability of the assembled battery. Moreover, the neutral aqueous ZAIBs can retain the advantages of high safety, environmental friendliness, and low manufacturing cost brought by typical ZABs, while also demonstrating superior cycle life and higher volumetric specific capacity (Figure 7h), strongly supporting their promising applications as highly sustainable energy storage systems.

3. Conclusions

In summary, this work presents highly reversible neutral aqueous ZAIBs for the first time, utilizing iodide-mediated oxygen redox chemistry. The neutral ZAIB device features honeycomb carbon loaded with FeN nanoparticles as a multifunctional catalyst and a KI-based neutral electrolyte, thus addressing the challenges of irreversible iodine oxidation in alkaline ZAIBs and

© 2025 Wiley-VCH GmbH

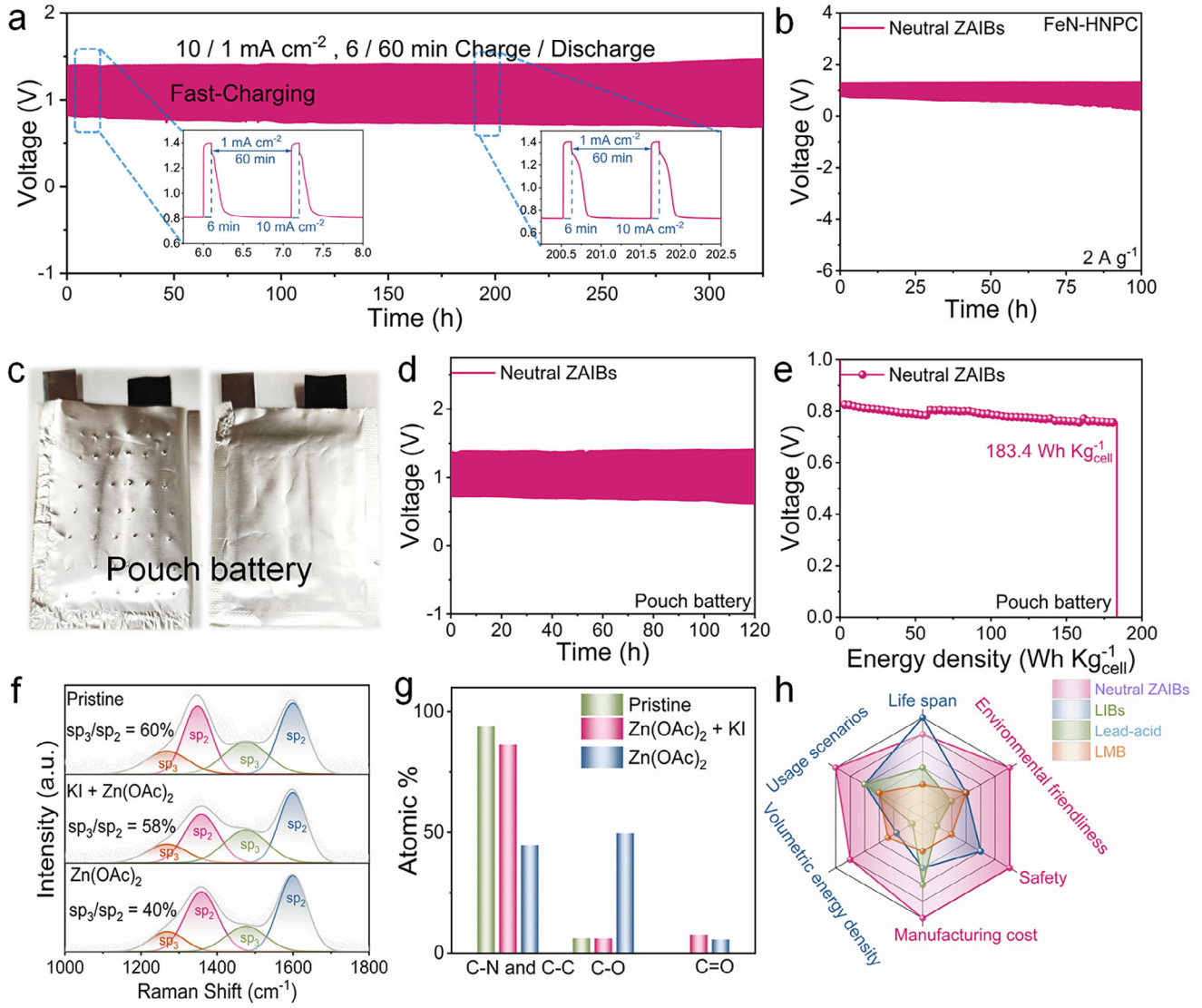

Figure 7. a) Fast charge cycling measurement (charge: 10 mA cm^{-2} for 6 min, discharge: 1 mA cm^{-2} for 60 min) for neutral ZAIBs. b) Galvanostatic discharge/charge profiles of coin-type ZAIBs using an 80 µL electrolyte at 2 A g^{-1} under air atmosphere. c) Photograph of the pouch battery. d) Galvanostatic discharge/charge profiles of pouch battery (electrode area of 25 cm^2). e) Energy density curves of pouch battery. f) Raman spectra of the FeN-HNPC catalyst before and after cycling on neutral ZABs and ZAIBs. g) The distribution of the corresponding fitted C species after cycling in different electrolytes. h) A comparison between neutral ZAIBs and other battery systems.

sluggish oxygen reaction kinetics coupled with insulating discharge byproduct accumulation in neutral environments. Mechanistic studies employing in situ UV–vis/Raman spectroscopy, FTIR, and pH monitoring reveal the closed-loop iodine-oxygen redox process in the neutral ZAIB system. Specifically, during discharge, I^- ions accelerate oxygen reduction and induce the formation of ZHA, resulting in higher discharge voltage. In the charge process, the low-potential IOR process dominates, wherein I^- is oxidized back to I_3^- and ZHA decomposes to release OH^-. The liberated OH^- spontaneously reacts with I_3^- to regenerate I^- and evolve O_2, thereby lowering charge voltage. This reversible iodide-oxygen cycle allows the neutral aqueous ZAIBs to operate with a low charge/discharge voltage gap of only 640.1 mV, a high round-trip energy efficiency of 54.0% and an ultralong cycle life of over 1800 h at 2 mA cm^{-2}, outperforming most previously reported neutral ZABs and even competing with traditional alkaline systems. The design of this advanced neutral ZAIB system expands the metal–air batteries family and offers new strategies for developing high-performance batteries in neutral electrolytes.

4. Experimental Section

Chemicals: $Fe(NO_3)_3{\cdot}9H_2O$, $Zn(NO_3)_2{\cdot}6H_2O$ was purchased from Shanghai Aladdin Chemical Reagents Co., Ltd. Other chemicals, such as absolute ethanol, tetraethyl orthosilicate, 4-aminoantipyrine, and KOH were obtained from Sinopharm Reagent Co., Ltd. All the reagents were directly used without further purification.

© 2025 Wiley-VCH GmbH

Synthesis of FeN-HNPC, FeN-NPC, and HNPC: In a typical procedure, 55 mL of absolute ethanol, 15 mL of deionized (DI) water, and 3 mL of tetraethyl orthosilicate were mixed homogeneously. Then, 4 mL of aqueous ammonia was added dropwise into the solution. The resulting mixture was centrifuged at 700 rpm, followed by washing and drying, to obtain SiO_2 nanospheres. A mixture of 0.4 g above SiO_2 nanospheres, 0.8 g 4-aminoantipyrine, 0.1 g $Fe(NO_3)_3{\cdot}9H_2O$, and 0.3 g $Zn(NO_3)_2{\cdot}6H_2O$ was dispersed in 20 mL of methanol. The solution was stirred at 80 °C until the methanol evaporated. The resulting solid was heated to 900 °C for 10 min in an inert N_2 atmosphere with a heating rate of 10 °C min^{-1}. SiO_2 was removed by washing with 3 M KOH solution at 80 °C. The product was centrifuged and washed with ethanol, and then thermally treated at 800 °C under N_2 atmosphere for 3 h at a ramping rate of 5 °C min^{-1} to obtain FeN-HNPC. The synthesis of FeN-NPC follows the same procedure as FeN-HNPC, except that SiO_2 is not used. Similarly, HNPC is synthesized without the addition of $Fe(NO_3)_3{\cdot}9H_2O$.

Preparation of Alkaline and Neutral Electrolytes: The alkaline and neutral electrolytes used in the ZABs assembled in this work were 6.0 M KOH + 0.2 M $Zn(OAc)_2$ and 1.0 M $Zn(OAc)_2$ electrolytes, respectively. To prepare the KI-based electrolyte, 1.0 M KI was used as the additive to dissolve in 6.0 M KOH + 0.2 M $Zn(OAc)_2$ and 1.0 M $Zn(OAc)_2$ solvent by magnetic stirring at 30 °C. The pH value of neutral aqueous electrolyte (1.0 M KI + 1.0 M $Zn(OAc)_2$) is about 5.6. The aforementioned KI-based electrolytes are used in the production of alkaline ZAIBs and neutral ZAIBs, respectively.

Characterizations: Powder XRD patterns were collected on a Bruker D8 Advance diffractometer with Cu-Kα radiation. SEM measurements were performed at a Hitachi S-4800 scanning electron microanalyzer with an accelerating voltage of 15 kV. TEM and HRTEM were conducted with a JEM-2100F field emission TEM at 200 kV. XPS measurements were recorded on an ESCALab MKII X-ray photoelectron spectrometer using Al Kα X-ray as the excitation source. Raman spectra were carried out on a Renishaw in Via-Refles with a laser line of 532 nm. N_2 adsorption–desorption tests were measured at 77 K with Quantachrome autosorb iQ. UV absorption spectroscopy (Evolution 300, USA) was employed to determine the concentration of I^- and I_3^-. In situ Raman spectra were collected on a Renishaw in Via-Refles with 533 nm laser excitation in O_2-saturated 0.1 M KOH + 1.0 M KI and 1.0 M $Zn(OAc)_2$ + 1.0 M KI at room temperature. Optical images were collected by an optical microscope (BX53MRF-S Japan), and the optical bench features a transparent electrolyte chamber made of acrylic sheets, which allows the electrode surface to be seen. XAFS spectroscopy was carried out using the RapidXAFS 2 M (Anhui Absorption Spectroscopy Analysis Instrument Co., Ltd.) by transmission (or fluorescence) mode at 20 kV and 20 mA, and the Si (733) spherically bent crystal analyzer with a radius of curvature of 500 mm was used for Fe.

Supporting Information

Supporting Information is available from the Wiley Online Library or from the author.

Acknowledgements

J.C. and W.L. contributed equally to this work. This work was financially supported by the National Natural Science Foundation of China (Nos. 22272150 and 52403392), Zhejiang Provincial Ten Thousand Talent Program (No. 2021R51009), Zhejiang Provincial Natural Science Foundation of China (No. LQ24B030013), Talent Start-up Project of Zhejiang A&F University Scientific Research Development Foundation (Nos. 2023LFR051 and 2024LFR003). The calculations were carried out on high performance supercomputer of Zhejiang Normal University. The authors thanked the Anhui Absorption Spectroscopy Analysis Instrument Co, Ltd. for XAFS measurements and analysis.

Conflict of Interest

The authors declare no conflict of interest.

Data Availability Statement

Research data are not shared.

Keywords

FeN nanoparticles, honeycomb porous carbon, I^-/I_3^- redox, neutral electrolyte, zinc–air/iodide hybrid batteries

Received: June 16, 2025
Revised: August 1, 2025
Published online:

[1] a) P. Tan, B. Chen, H. Xu, H. Zhang, W. Cai, M. Ni, M. Liu, Z. Shao, *Energy Environ. Sci.* **2017**, *10*, 2056; b) Z. Xu, J. Chen, T. Zhang, H. Lu, L. Yan, J. Ning, Y. Hu, *Adv. Energy Mater.* **2025**, *15*, 2402839.
[2] a) S. Jin, P. Y. Chen, Y. Qiu, Z. Zhang, S. Hong, Y. L. Joo, R. Yang, L. A. Archer, *J. Am. Chem. Soc.* **2022**, *144*, 19344; b) H. Xia, R. Pang, X. Dong, Q. Liu, J. Chen, E. Wang, J. Li, *J. Am. Chem. Soc.* **2023**, *145*, 25695.
[3] Q. Wang, S. Kaushik, X. Xiao, Q. Xu, *Chem. Soc. Rev.* **2023**, *52*, 6139.
[4] a) L. Yan, J. Chen, C. Yang, J. Ning, Y. Hu, *Small Sci* **2023**, *4*, 2300094; b) Z. Song, J. Ding, B. Liu, X. Liu, X. Han, Y. Deng, W. Hu, C. Zhong, *Adv. Mater.* **2020**, *32*, 1908127.
[5] a) S. Zhao, T. Liu, Y. Dai, J. Wang, Y. Wang, Z. Guo, J. Yu, I. T. Bello, M. Ni, *Appl. Catal. B - Environ.* **2023**, *320*, 121992; b) I. Temprano, T. Liu, E. Petrucco, J. H. J. Ellison, G. Kim, E. Jónsson, C. P. Grey, *Joule* **2020**, *4*, 2501.
[6] A. Wang, X. Zhang, S. Gao, C. Zhao, S. Kuang, S. Lu, J. Niu, G. Wang, W. Li, D. Chen, H. Zhang, X. Zhou, S. Zhang, B. Zhang, W. Wang, *Adv. Mater.* **2022**, *34*, 2204247.
[7] Q. Liu, C. Xia, C. He, W. Guo, Z. P. Wu, Z. Li, Q. Zhao, B. Y. Xia, *Angew. Chem., Int. Ed.* **2022**, *61*, 202210567.
[8] a) Y. Tang, Y. Li, Z. Yu, Y. Bai, Y. Chen, Y. Sun, P. Wan, *Green Chem.* **2012**, *14*, 334; b) W. Zhang, J. Zhang, N. Wang, K. Zhu, C. Yang, Y. Ai, F. Wang, Y. Tian, Y. Ma, Y. Ma, X. Zhang, L. Duan, D. Chao, F. Wang, D. Zhao, W. Li, *Nat. Sustainability* **2024**, *7*, 463.
[9] J. Qiao, Y. You, L. Kong, W. Feng, H. Zhang, H. Huang, C. Li, W. He, Z. Sun, *Adv. Mater.* **2024**, *36*, 2405533.
[10] M. Cui, N. Ma, H. Lei, Y. Liu, W. Ling, S. Chen, J. Wang, H. Li, Z. Li, J. Fan, Y. Huang, *Angew. Chem., Int. Ed.* **2023**, *62*, 202303845.
[11] S. Clark, A. R. Mainar, E. Iruin, L. C. Colmenares, J. A. Blázquez, J. R. Tolchard, Z. Jusys, B. Horstmann, *Adv. Energy Mater.* **2020**, *10*, 1903470.
[12] a) W.-F. Wu, X. Yan, Y. Zhan, *Chem. Eng. J.* **2023**, *451*, 138608; b) Y.-f. Cui, Y.-h. Zhu, J.-y. Du, Y.-l. Zhang, K. Li, W.-q. Liu, G. Huang, X.-b. Zhang, *Joule* **2022**, *6*, 1617; c) Y. Shao, W. Lu, T. Zhang, B. Yin, B.-B. Xie, J. Ning, Y. Hu, *Carbon Energy* **2025**, *7*, 701.
[13] W. Sun, F. Wang, B. Zhang, M. Zhang, V. Küpers, X. Ji, C. Theile, P. Bieker, K. Xu, C. Wang, M. Winter, *Science* **2021**, *371*, 46.
[14] W. Sun, V. Kupers, F. Wang, P. Bieker, M. Winter, *Angew. Chem., Int. Ed.* **2022**, *61*, 202207353.
[15] a) M. Liu, Q. Chen, X. Cao, D. Tan, J. Ma, J. Zhang, *J. Am. Chem. Soc.* **2022**, *144*, 21683; b) Z. Li, S. Ning, J. Xu, J. Zhu, Z. Yuan, Y. Wu, J. Chen, F. Xie, Y. Jin, N. Wang, H. Meng, S. Sun, *Energy Environ. Sci.* **2022**, *15*, 5300.
[16] H. Chen, X. Li, K. Fang, H. Wang, J. Ning, Y. Hu, *Adv. Energy Mater.* **2023**, *13*, 2302187.
[17] Z. Wang, Z. Lu, Q. Ye, Z. Yang, R. Xu, K. Kong, Y. Zhang, T. Yan, Y. Liu, Z. Pan, Y. Huang, X. Lu, *Adv. Funct. Mater.* **2024**, *34*, 2315150.
[18] Y. Wang, X. Jin, J. Xiong, Q. Zhu, Q. Li, R. Wang, J. Li, Y. Fan, Y. Zhao, X. Sun, *Adv. Mater.* **2024**, *36*, 2404093.

© 2025 Wiley-VCH GmbH

[19] D. Kundu, B. D. Adams, V. Duffort, S. H. Vajargah, L. F. Nazar, *Nat. Energy* **2016**, *1*, 16119.
[20] L. Zhou, Y. Yang, J. Yang, P. C. Ye, T. Ali, H. Y. Wang, J. Q. Ning, Y. J. Zhong, Y. Hu, *Appl. Surface Sci.* **2022**, *604*, 154526.
[21] a) K. B. Chen, T. T. Wang, Z. W. Xu, N. Tian, J. Cai, W. Y. Qiu, B. Zhang, Z. Yin, B. Liu, M. H. Zeng, *Aggregate* **2025**, *6*, 70094. b) X. Liu, H. Liu, C. Chen, L. Zou, Y. Li, Q. Zhang, B. Yang, Z. Zou, H. Yang, *Nano Res.* **2019**, *12*, 1651; c) Q. Lai, H. Zheng, W. Zhang, Y. Sheng, L. Nie, J. Zheng, *Nanoscale* **2023**, *15*, 16188.
[22] S. J. Kim, J. Mahmood, C. Kim, G. F. Han, S. W. Kim, S. M. Jung, G. Zhu, J. J. De Yoreo, G. Kim, J. B. Baek, *J. Am. Chem. Soc.* **2018**, *140*, 1737.
[23] L. Zong, K. Fan, L. Cui, F. Lu, P. Liu, B. Li, S. Feng, L. Wang, *Angew. Chem., Int. Ed.* **2023**, *62*, 202309784.
[24] J. Chen, C. Qiu, L. Zhang, B. Wang, P. Zhao, Y. Zhao, H. Wang, G. Yang, A. Sun, J. Fan, Q. Xv, O. J. Rojas, *Energy Environ. Sci.* **2024**, *17*, 4746.
[25] C. Liu, R. Yang, J. Wang, B. Liu, X. Chang, P. Feng, X. Zhang, L. Zhong, X. Zhao, L. Niu, S. Gan, Y. Xi, M. Huang, H. Wang, *Angew. Chem., Int. Ed.* **2025**, *64*, 202501266.
[26] L. Peng, J. Yang, Y. Yang, F. Qian, Q. Wang, D. Sun-Waterhouse, L. Shang, T. Zhang, G. I. N. Waterhouse, *Adv. Mater.* **2022**, *34*, 2202544.
[27] M. Thommes, K. Kaneko, A. V. Neimark, J. P. Olivier, F. Rodriguez-Reinoso, J. Rouquerol, K. S. W. Sing, *Pure Appl. Chem.* **2015**, *87*, 1051.
[28] Z. Li, S. Ji, C. Xu, L. Leng, H. Liu, J. H. Horton, L. Du, J. Gao, C. He, X. Qi, Q. Xu, J. Zhu, *Adv. Mater.* **2023**, *35*, 2209644.
[29] Q. Tian, L. Jing, H. Du, Y. Yin, X. Cheng, J. Xu, J. Chen, Z. Liu, J. Wan, J. Liu, J. Yang, *Nat. Commun.* **2024**, *15*, 983.
[30] W. Cai, J. Geng, S. Zhao, Y. Zhu, Y. Wang, Q. Chen, K. Guo, *Electrochem. Commun.* **2023**, *151*, 107494.
[31] Y. Yan, S. Liang, X. Wang, M. Y. Zhang, S.-M. Hao, X. Cui, Z. W. Li, Z. Q. Lin, *Proc. Natl. Acad. Sci. USA* **2021**, *118*, 2110036118.
[32] J. Liu, Q. Ye, Y. Wu, J. L. Chen, Y. J. Ge, L. J. Zhang, R. Abazari, J. J. Qian, *Sci. China Chem.* **2025**, *68*, 1859.
[33] a) H. Zhang, H.-C. Chen, S. Feizpoor, L. Li, X. Zhang, X. Xu, Z. Zhuang, Z. Li, W. Hu, R. Snyders, D. Wang, C. Wang, *Adv. Mater.* **2024**, *36*, 2400523; b) L. Yang, X. Zhang, L. Yu, J. Hou, Z. Zhou, R. Lv, *Adv. Mater.* **2022**, *34*, 2105410.
[34] K. Ding, J. Hu, L. Zhao, W. Jin, H. Yu, Y. Liu, Z. Wu, S. Cai, Y. Yang, G. Zou, H. Hou, X. Ji, *Nano Energy* **2024**, *121*, 109270.
[35] R. Kapaev, M. Noked, *Chem. Commun.* **2023**, *59*, 9856.
[36] Y. N. Zhang, H. L. Qin, M. Alfred, H. Z. Ke, Y. B. Cai, Q. Q. Wang, F. L. Huang, B. Liu, P. F. Lv, Q. F. Wei, *Energy Storage Mater.* **2021**, *42*, 88.
[37] C. L. Zhu, Z. X. Yin, W. H. Lai, Y. Sun, L. N. Liu, X. T. Zhang, Y. J. Chen, S.-L. Chou, *Adv. Energy Mater.* **2018**, *8*, 1802327.
[38] S. J. Xu, A. R. Dong, Y. Hu, Z. Yang, S. M. Huang, J. J. Qian, *J. Mater. Chem. A* **2023**, *11*, 9721.
[39] L. Ma, Y. Ying, S. Chen, Z. Huang, X. Li, H. Huang, C. Zhi, *Angew. Chem., Int. Ed.* **2021**, *60*, 3791.
[40] T. T. Liu, H. J. Wang, C. J. Lei, Y. Mao, H. Q. Wang, X. He, X. Liang, *Energy Storage Mater.* **2022**, *53*, 544.
[41] M. Wang, Y. Meng, M. Sajid, Z. Xie, P. Tong, Z. Ma, K. Zhang, D. Shen, R. Luo, L. Song, L. Wu, X. Zheng, X. Li, W. Chen, *Angew. Chem., Int. Ed.* **2024**, *39*, 202404784.
[42] L. Ma, S. Chen, Z. Pei, H. Li, Z. Wang, Z. Liu, Z. Tang, J. A. Zapien, C. Zhi, *ACS Nano* **2018**, *12*, 8597.
[43] L. Chai, J. Song, N. Jiang, X. Liu, Y. Sun, X. Li, J. Pan, *Adv. Funct. Mater.* **2025**, *35*, 2504059.
[44] Z. Chen, F. Wang, R. Ma, W. Jiao, D. Li, A. Du, Z. Yan, T. Yin, X. Yin, Q. Li, X. Zhang, N. Yang, Z. Zhou, Q.-H. Yang, C. Yang, *ACS Energy Lett.* **2024**, *9*, 2858.
[45] A. Moezzi, A. McDonagh, A. Dowd, M. Cortie, *Inorg. Chem.* **2013**, *52*, 95.
[46] a) H. R. Liu, G. X. Shao, W. Jia, Z. X. Zhang, Y. Zhang, J. Liang, X. G. Liu, H. S. Jia, B. S. Xu, *CrystEngComm* **2013**, *15*, 3615; b) Z. Xia, Y. Wang, Y. Fang, Y. Wan, W. Xia, J. Sha, *J. Phys. Chem. C* **2011**, *115*, 14576.
[47] X. Bi, J. Li, M. Dahbi, J. Alami, K. Amine, J. Lu, *Adv. Mater.* **2022**, *34*, 2106148.
[48] a) B. Zhou, L. Guo, Y. Zhang, J. Wang, L. Ma, W.-H. Zhang, Z. Fu, Z. Peng, *Adv. Mater.* **2017**, *29*, 1701568; b) C. He, J. Lei, X. Li, Z. Shen, L. Wang, J. Zhang, *Angew. Chem., Int. Ed.* **2024**, *63*, 202406143; c) Y. Feng, S. Luo, A. Duan, M. Li, B. Zhang, W. Sun, *Adv. Energy Mater.* **2025**, *15*, 2501294.
[49] D. Xu, B. Chen, X. Ren, C. Han, Z. Chang, A. Pan, H. Zhou, *Energy Environ. Sci.* **2024**, *17*, 642.
[50] R. H. Jiang, T. Naren, Y. J. Chen, Z. Chen, C. X. Zhang, L. Ma, H. K. Xu, L. B. Chen, L. J. Zhou, W. F. Wei, *Energy Storage Mater.* **2023**, *63*, 103044.
[51] a) Q. Chen, K. Ouyang, Y. Wang, M. Chen, H. Mi, J. Chen, C. He, H. Li, D. Ma, P. Zhang, *Adv. Funct. Mater.* **2024**, *34*, 2406386; b) L. Tang, H. J. Peng, J. R. Kang, H. Chen, M. Y. Zhang, Y. Liu, D. H. Kim, Y. J. Liu, Z. Q. Lin, *Chem. Soc. Rev.* **2024**, *53*, 4877.
[52] a) C. Tian, J. Wang, R. Sun, T. Ali, H. Wang, B. B. Xie, Y. Zhong, Y. Hu, *Angew. Chem., Int. Ed.* **2023**, *62*, 202310970; b) H. Wang, W. Ye, B. Yin, K. Wang, M. S. Riaz, B. B. Xie, Y. Zhong, Y. Hu, *Angew. Chem., Int. Ed.* **2023**, *62*, 202218872.
[53] a) A. Wang, X. Zhang, S. Gao, C. Zhao, S. Kuang, S. Lu, J. Niu, G. Wang, W. Li, D. Chen, H. Zhang, X. Zhou, S. Zhang, B. Zhang, W. Wang, *Adv. Mater.* **2022**, *34*, 2204247; b) Z. Xu, C. Jiao, Z. Shu, Y. Xia, S. Chen, S. Chen, H.-L. Wang, *Chem. Eng. J.* **2024**, *481*, 148798.
[54] S. Dongmo, D. Stock, J. J. Alexander Kreissl, M. Gross, S. Weixler, M. Hagen, K. Miyazaki, T. Abe, D. Schroder, *ACS Omega* **2020**, *5*, 626.
[55] S. S. Shinde, J. Y. Jung, N. K. Wagh, C. H. Lee, D.-H. Kim, S.-H. Kim, S. U. Lee, J.-H. Lee, *Nat. Energy* **2021**, *6*, 592.
[56] S. Q. Wu, X. B. Liu, H. M. Mao, T. Cui, B. Li, G. Z. Zhou, L. Wang, *Appl. Catal. B - Environ.* **2023**, *330*, 122634.
[57] X. Yao, Y. Zhu, T. Xia, Z. Han, C. Du, L. Yang, J. Tian, X. Ma, J. Hou, C. Cao, *Small* **2023**, *19*, 2301075.

 © 2025 Wiley-VCH GmbH